ANALYSIS OF
15 DECEMBER 2000 AND 3 FEBRUARY 2002
SULTANDAĞI-AFYON EARTHQUAKES

By
Doğan AKSARI
B.S. Geophysical Engineering, İstanbul Technical University, 2001

Submitted to
Boğaziçi University
Kandilli Observatory and Earthquake Research Institute
in partial fulfillment of
the requirements for the degree of
Master of Science
in Geophysics

Boğaziçi University
June 2006

ACKNOWLEDGEMENTS

I wish to express my deepest gratitude to my advisor Assoc. Prof. Hayrullah Karabulut for his valuable advices and guidance of this work. Special thanks and gratitude to Esen Arpat, Prof. Mustafa Aktar and Assoc. Prof. Serdar Özalaybey for their genuine support, valuable advice and sincere comments, which helped me a lot to finish this study. The Kandilli Observatory and Earthquake Research Institute, at the Boğaziçi University, and TÜBİTAK-Marmara Research Center provided support, including data, laboratory and office work.

I also want to express my gratitude to the department members, staff, and students of the Department of Geophysics and the members of the Kandilli Observatory and Earthquake Research Institute, Boğaziçi University.

I am deeply indebted to my friend Tuğce Afacan Ergün whose assistance and encouragement made this work possible towards the end.

Finally, I am particularly grateful to my family, for helping and assisting me in all the stages of this work. Without their help, this study would never have been possible. Special thanks to my mother and father for their patience and support.

Doğan AKSARI

June 2006

ABSTRACT

We analyzed two moderate size of earthquakes (M_w=6.0, M_w=6.5) occurred in Sultandağı-Afyon, southwestern Turkey on December 15, 2000 and February 3, 2002. Both earthquakes took place on the Sultandağı fault (SF) having normal mechanism with slightly different orientations and same directivities. Both earthquakes ruptured to the northwest of SF. The distance between the epicenters of two events was less than 16 km. We relocated the large magnitude aftershocks and used the closest broadband station (ISP – Isparta Station) to reveal the differences in the directivity. Coulomb stress changes for December 15, 2000 earthquake were calculated and its effect on February 3, 2002 event was explored. It was observed that the December 15, 2000 event increased Coulomb stress up to 4 bar in the area of February 3, 2002 and favored the 2002 rupture. Following both earthquakes, we observed seismic activity triggered in 40 km far from the first mainshock and 25 km from the second. It is considered that the activity took place as a result of dynamic triggering.

ÖZET

Türkiye'nin güneybatısında yer alan Sultandağı Afyon bölgesinde 15 Aralık 2000 ve 3 Şubat 2002 tarihlerinde (M_w=6.0, M_w=6.5) iki adet orta büyüklükte deprem olmuştur. Her iki deprem de Sultandağı Fayı üzerinde yer almıştır. Fay mekanizma çözümleri, yönü ve doğrultusu az miktarda farklı olmakla birlikte her iki depremin de normal faylanmaya sahip olduğunu göstermektedir. 2000 depreminin yırtılma yönü baskın olarak kuzeybatı yönündedir ancak 2002 depreminin yırtılma yönü tam olarak kuzeybatı yönündedir. İki depremin merkez üssü arasında 16 km'den az uzaklık bulunmaktadır. Yönelimdeki farkı göstermek için ISP (Isparta) geniş bantlı istasyona yakın büyük magnitüdlü artçı şokların lokasyonları yeniden yapılmıştır. 15 Aralık 2000 depremi için Coulomb stres değişimi ve depremin 3 Şubat 2002 depremine etkisi araştırılmıştır. 2000 depreminin 2002 depremini kırık alanına 4 bar'a kadar stres yüklemesi yaptığı gözlenmiştir. Her iki depremden sonra da birinci depremden 40, ikinci depremden 25 km uzakta kuzeybatı yönünde bir sismik aktivite gözlemlenmiştir. Bu aktivitenin dinamik tetikleme olduğu düşünülebilir.

TABLE OF CONTENTS

LIST OF FIGURES

LIST OF TABLES

LIST OF SYMBOLS

$\sim$	: Approximate
M_b	: Body Magnitude
M_L	: Local Magnitude
MPa	: Mega Pascal (= 10 bar)
M_S	: Surface Magnitude
M_w	: Moment Magnitude
ΔCFS	: Change in Coulomb Failure Stress
θ	: Angle between X Axis and the Greatest Principle Stress
μ	: Coefficient of Friction
μ'	: Effective Coefficient of Friction
σ_1	: Greatest Principles Stress
σ_2	: Intermediate Principles Stress
σ_3	: Smallest Principles Stress
σ_f	: Coulomb Stress
σ_n	: Normal Stress on the Failure Plane
σ_{ij}	: Component of Stress Tensor
τ_β	: Shear Stress on the Failure Plane
υ	: Poisson's ratio
ψ	: Angle between x Axis and Failure Plane

ABBREVIATIONS

EAF	: East Anatolian Fault
FORTRAN	: Formula Translation
GE	: GEOFON Network Code
GPS	: Global Positioning System
IRIS	: The Incorporated Research Institutions for Seismology
IS	: Israel Seismic Network
ISC	: International Seismology Center
ISP	: Isparta-Turkey Seismic Station Code
IU	: IRIS Network Code
KO	: Kandilli Observatory Network Code
KOERI	: Kandilli Observatory and Earthquake Research Center
MRC	: Marmara Research Center
NAF	: North Anatolian Fault
NEIC	: National Earthquake Information Center
TÜBİTAK	: The Scientific & Technological Research Council of Turkey
USGS	: United States Geological Survey
S-1	: The 2000 Sultandağı-Afyon Earthquake (Mw 6.0)
S-2	: The 2002 Sultandağı-Afyon Earthquake (Mw 6.5)
S-3	: The 2002 Sultandağı-Afyon Earthquake (Mw 5.8)

1. INTRODUCTION

Recent observational and theoretical studies indicate increasing evidences on triggering of earthquakes by other earthquakes. In order to have a better understanding of the earthquake triggering, it is important to examine the correlation between the stress changes, caused by large earthquakes and the associated seismicity rate changes in regions usually identified as the aftershock zone (Kilb et al., 2002). Many of these studies show positive correlations between the spatial distributions of aftershocks, or sequences of moderate to large events, with modeled changes in static Coulomb failure stresses (ΔCFS) generated by earlier nearby large earthquakes (Gomberg et al., 1998). The observed correlation between ΔCFS and triggered earthquakes appear to require time-dependent fault strength and/or additional delaying mechanism because of the commonly observed delay between the triggering and triggered earthquakes (Gomberg et al., 1998). These observations are consistent with Coulomb failure if the static stress change brings a prestressed fault closer to failure and the background tectonic loading finishes off the job.

On the other hand, the simple Coulomb stress failure criterion does not account for all of the observations of triggered seismicity. Coulomb failure analysis only allows delayed triggered seismicity to be induced by a change in the static stress field, whereas long-range interactions between earthquakes have also been observed where static stress changes are negligible (Hill et al., 1993). The increased seismicity observed in areas following a large earthquake where the static Coulomb stress is negligible led many scientist to consider the transient deformations (i.e., due to seismic waves) triggered the remote earthquakes (Hill et al., 1993; Gomgerg, 1996).

Man-made earthquake triggering has been recognized (e.g., Carder, 1945; Healy et al., 1968; Kovach, 1974; Raleigh et al., 1972,1976; Segall, 1992; McGarr and Simpson, 1997) as a result of the activities such as fluid injection and withdrawal, mining and hydrocarbon recovery (Harris, 1998). Calculation of static stress changes affecting subsequent earthquake location are presented by Smith and Van de Lindt (1969), Rybicki (1973), Yamashina (1978), Das and Scholz (1981) and Stein and Lisowski (1983).

However, since stress changes were very small, the scientific community ignored the earthquakes triggered by earthquakes for a long time.

However, with the increasing quality and quantity of seismological observations around the world many examples of triggering have been presented. It has been accepted now that while each event produces a net reduction of regional stress, events also result in stress increases (King et al., 1994). With further tectonic loading, such sites of stress rise should be the foci of future events. If this mechanism works well, every point of brittle crust is a point of failure and every earthquake can trigger nearby or distant earthquakes. Although triggering has not been observed as widely as expected phenomena such as, the steady migration of epicenters along the North Anatolian (Ambraseys, 1970) and San Jacinto (Sanders, 1993) faults are considered as typical examples.

Majority of the works related to Coulomb stress analysis have focused on strike-slip faults, such as the San Andreas, North Anatolian, and eastern California shear zone; or on normal faults in western Turkey, Greece, Italy and the U.S. Basin and Range province (see reviews by Harris (1998), Stein (1999), King and Cocco (2000), and Stein (2003)). Both Stein et al. (1997) and Nalbant et al. (1998) identified the İzmit Bay area in western Turkey as being of particularly high earthquake risk. About after one year, this region faced with a devastating magnitude M_w=7.4 earthquake in 1999. In addition, after a short time of 1999 earthquake, Barka noted increased loading on fault segments at either end of rupture; Bolu-Düzce segment failed 3 months later in an M_w=7.1 event (Nalbant et al., 2002).

Hillers (2001) studied the aftershock sequences of the 1999 Izmit and Düzce earthquakes and showed interactions between two. He obtained the Coulomb stress change field of the Izmit shock which is in agreement by Parsons et al. (2000), Hubbert-Ferrari et al. (2000) and Pınar et al. (2001), by using a different source model. He observed that Düzce epicenter was loaded by 0.2 MPa due to the Izmit mainshock.

Utkucu et al., (2003) studied the slip distribution and stress changes associated with the 12 November 1999, Düzce earthquake. They modeled static stress changes of earthquakes from 1943 and this calculation suggests that the Düzce earthquake was triggered as a result of the 17 August 1999 İzmit earthquake, which changed the stress state

at the hypocentre location from negative to positive. However, they found that the calculated slip distribution during the Düzce earthquake does not correspond with the mapped stress change anomalies on the fault surface. They thought that this result causes the lack of correlation between stress and slip. Because much of the rupture plane of the Düzce earthquake experienced a positive Coulomb stress change, they concluded that this is clearly consistent with Coulomb triggering. In conclusion, they resulted that the stress modeling indicates that the northern branch of the North Anatolian fault zone, beneath the Sea of Marmara towards the city of İstanbul, is presently the most highly loaded segment of the North Anatolian Fault Zone.

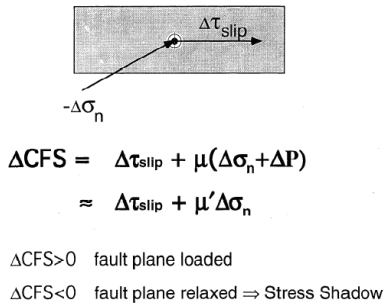

Figure 1.1 ΔCFS, the change in Coulomb failure stress, or Coulomb stress increment, is used to evaluate if one earthquake brought another earthquake closer to, or farther from, failure. If ΔCFS > 0, the first earthquake brought the second earthquake closer to failure; if ΔCFS < 0, the first event sent the second event farther away from failure and into a stress shadow. (Harris, 1998)

Another good example of Coulomb stress changes study is the 1992 M 7.4 Landers and 1992 M 6.5 Big Bear earthquakes. Many scientists studied this interaction. Stein et al., 1994 found that the distribution of aftershocks for the Landers earthquake, as well as for several other moderate events in its vicinity, can be explained by the Coulomb criterion. They found that several moderate shocks raised the stress at the future Landers epicenter and along much of the Landers rupture zone by about a bar, advancing the Landers shock by 1-3 centuries. They reported that the Landers rupture, increased the stress at site of the future M=6.5 Big Bear aftershock site by 3 bars. Then they used the same procedure to resolve stress changes on the San Andreas and San Jacinto faults imposed by the Landers sequence. They have another conclusion that together the Landers and Big Bear earthquakes raised the stress along the San Bernardino segment of the southern San Andreas Fault by 2-6 bars, hastening the next great earthquake there by about a decade. (Stein et al., 1994)

A few number of studies on Coulomb stress analysis on the normal faults have been performed. Nostro et al. (2005) investigated fault interaction through elastic stress transfer among a sequence of moderate-size earthquake ($5 < M_w < 6$) which ruptured distinct normal fault segments during a seismic sequence in the Umbria-Marche region (central Apennines). The modeling results show that seven out of eight main shocks of the sequence occurred in areas of enhanced Coulomb stress, implying that elastic stress transfer may have promoted the occurrence of these moderate- size events. 82% of aftershocks are located in areas of positive stress changes for optimally oriented planes. However only half of the fault plane solutions computed from polarity data are consistent with the focal mechanisms associated with the optimally oriented planes. Their interpretation of their modeling results is that elastic stress transfer alone cannot jointly explain the aftershock spatial distribution and their focal mechanism (Nostro et al., 2005).

Payne et al., (2004) investigated interaction between the 1984 Devil Canyon M_L 5.8, 1983 M_s 7.3 Borah Peak, Idaho, and 1984 M_L 5.0 Lone Pine earthquakes. They thought that 1984 Devil Canyon sequence was a late aftershock sequence of the Borah Peak, Idaho earthquake. The 1983 Borah Peak mainshock triggered the 1984 Devil Canyon sequence that was associated with conjugate normal faulting along the Challis segment of the Lost River fault system and Lone Pine faults. The Devil Canyon hypocenters show two planar faults that form a "V" structure in the brittle upper crust from 5 to 13 km depth. Temporal aspects of the Devil Canyon sequence provide strong evidence that slip on conjugate normal faults occurs sequentially. Aftershocks of the Devil Canyon sequence occurred immediately northwest of the M_L 5.8 Devils Canyon earthquake, which itself was immediately northwest of the Thousand Springs segment of the Lost River fault (the fault that slipped in association with the M_s 7.3 Borah Peak earthquake). They reported that Coulomb failure stress analysis indicates that stress increases resulting from both the Borah Peak mainshock and Devil Canyon M_L 5.8 earthquake were sufficient to induce failure on the Lone Pine fault. As a conclusion, they suggested that conjugate normal faults may transfer stress or accommodate stress changes at the terminations of major normal faults in the Basin and Range Province.

On 15 December 2000 an earthquake of M_w=6.0 occurred in the Sultandağı, Afyon, the southwestern Turkey (38.402°, 31.325°). The rupture took place on the southeastern segment of the Sultandağı fault. The mechanism of the earthquake shows a normal faulting

with a strike direction 285°. Two years later, on 3 February 2002 another earthquake of Mw=6.5 occurred on the northwestern segment of the Sultandağı fault (38.52°, 31.20°). The mechanism of the 2002 earthquake was normal faulting similar to the 2000 event with slightly different orientation (Strike: 269°). The distance between two earthquakes was approximately 16 km and the rupture directions were nearly the same, unilaterally propagating to the northwest of the fault. We relocated the large aftershocks of both events and observed that the aftershock distributions define a fault length of 25 km for the 2000 event and 40 km for the 2002 events. The results are consistent with the seismic moment of the earthquakes. The aftershocks also indicate a triggered seismicity in the area of *Kızıldağ* after several days of 2000 event and few hours later from 2002 mainshock. The observed seismicity at the northwestern extremity of the Sultandağı fault is considered the result of dynamic triggering.

The purpose of this study is to investigate if there is an interaction between 2000 and 2002 events. We used Coulomb Failure Criteria to reveal this probable interaction. We observed up to 4 bars increase on the stress in the area of 2002 mainshock as a result of the 2000 event.

2. TECTONIC SETTING

The collision of the Arabian plate and the Eurasian plate (Figure 2.1) along a localized collision front controls the tectonic escape of the Anatolian plate (Barka and Kandinsky-Cade, 1988). This movement was accomplished along two major strike-slip faults, the right lateral North Anatolian Fault (NAF) and the left-lateral East Anatolian Fault (EAF). The right-lateral NAF extends for 1000 km from eastern Turkey to Aegean Sea in an arc parallel to the Black Sea coast (Ketin, 1948). Over much of its length, the fault is simple and single structure. In western Turkey, the fault splits into two main strands in the Marmara region and its passage across the Aegean is more complicated.

North Aegean and western Turkey are currently undergoing a continental lithospheric extension in the NS direction (McKenzie, 1973; Angelier, 1978; McKenzie, 1978; LePichon and Angelier, 1981; Şengör et al., 1984). However, different views exist on the explanation of the driving mechanism of this extension process. Some authors associate the extension with slab pull of retreating Hellenic Subduction Zone (McKenzie, 1978; LePichon and Angelier, 1981). Others (McKenzie, 1978; Dewey and Şengör, 1979; Taymaz et al., 1991) declare the interaction of the Arabian plate with Eurasia and the apparent extrusion of Anatolia towards the west from the zone of most intense convergence.

GPS studies during the last two decades shed light on some of the questions related to the motion of the plates involved in the regional tectonics. Reilinger et al. (2006) studied secular velocity field for the period 1988-2005 in the zone of interaction of the Nubian, Somalian, Arabian and Eurasian plates. They found that the velocity field (Figure 2.2) indicates counterclockwise rotation of a broad area including the Arabian, Anatolian, and Aegean regions and adjacent parts of the Zagros and central Iran. Rates of motion associated with this rotation increase towards the Hellenic-Cyprus trench system. According to Reilinger et al. (2006), this increasing rate of motion towards the Hellenic and Cyprus trenches suggests that the primary forces responsible for westward motion of

Anatolia, and perhaps counterclockwise rotation of Arabia, are associated with slab rollback along the Hellenic and Cyprus trenches.

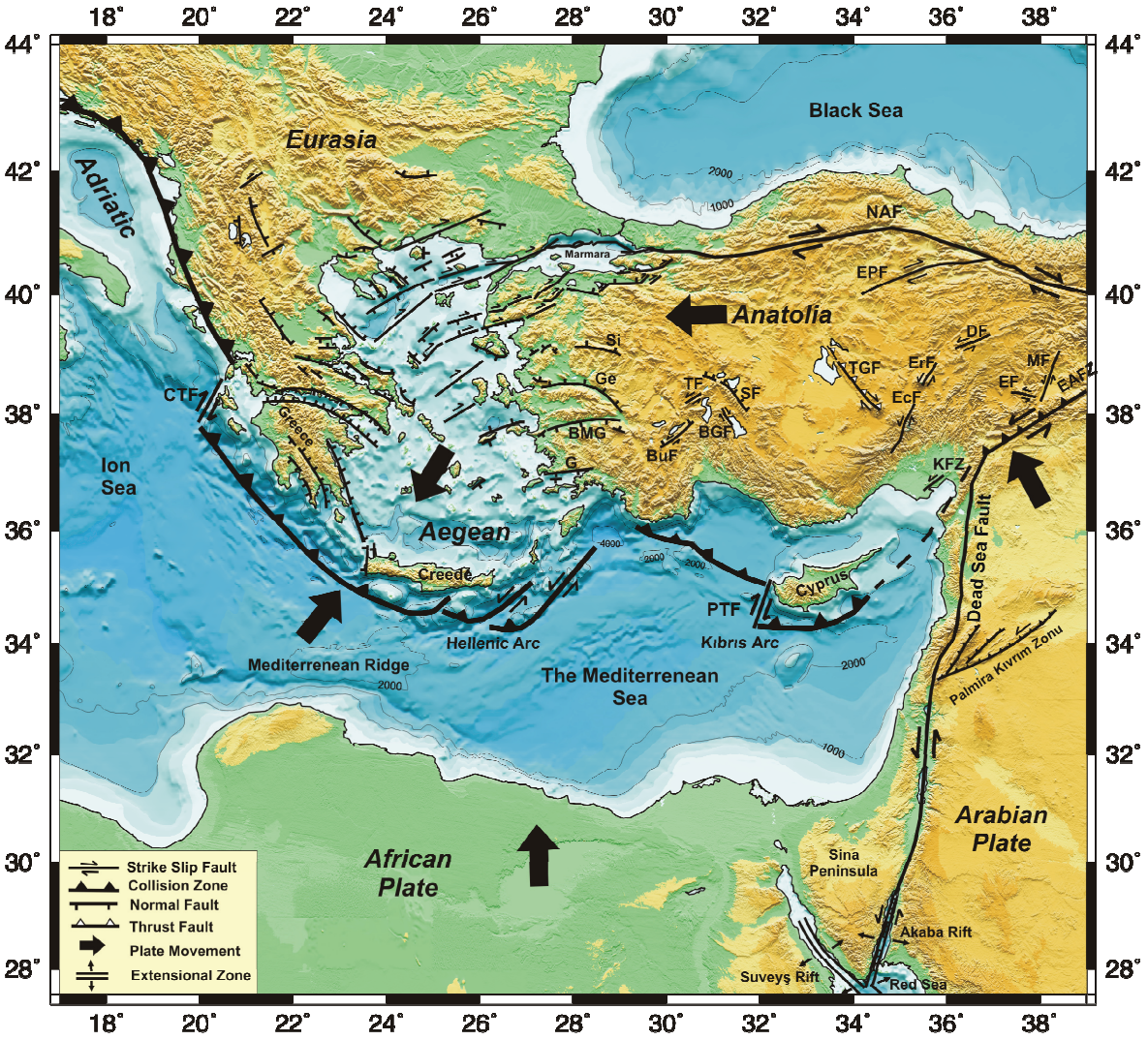

Figure 2.1 Tectonic map of the eastern Mediterranean region. The large black arrows show current relative motions in western Turkey and eastern Mediterranean, and the smaller half arrows are the directions of movement on major strike–slip faults. (after Taymaz et al., 2002)

The region of the present study in the vicinity of the city of Afyon and close to the apex of the Isparta Angle is shown in the Figure 2.3 with major faults delineating Afyon-Akşehir graben.

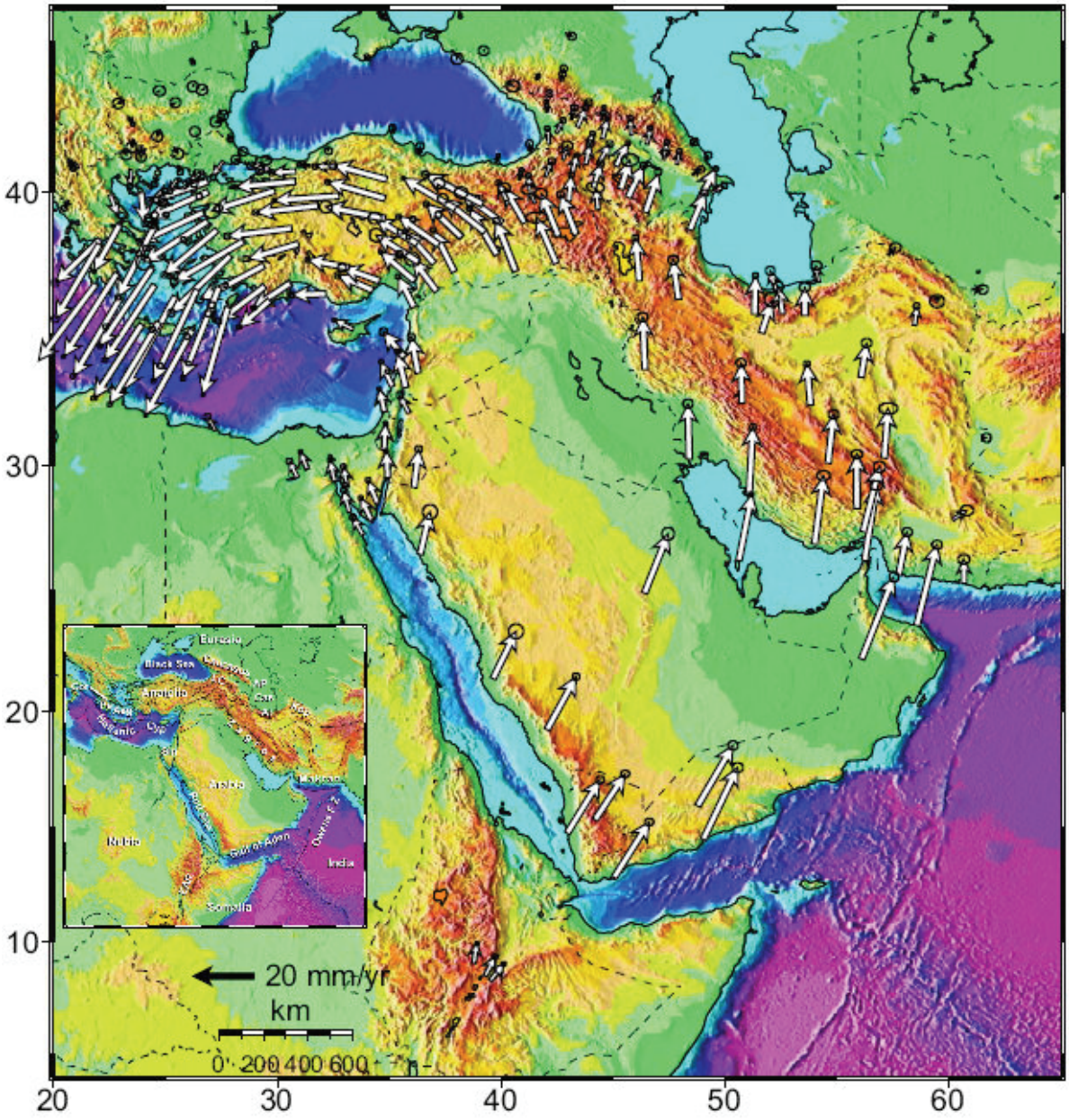

Figure 2.2 GPS horizontal velocities and their 95% confidence ellipses in a Eurasia-fixed reference frame for the period 1988-2005 (after Reilinger et al., 2006).

The main tectonic features of central Isparta Angle region are illustrated in Figure 2.3. Extensive investigations have shown that, numerous grabens systems have been forming in the E-W and WNW-ESE directions due to the N-S substantial extension in western Anatolia (Ketin 1968; Dewey and Şengör 1979; Jackson and Mc Kenzie, 1984). Gökova, Büyük Menderes, Küçük Menderes, Gediz, Bakırçay, Kütahya, Eskişehir and Simav Grabens constitute the main tectonic structure of the region together with Tuzla and Bergama-Foça fault zones trending in NE-SW direction. A number of major normal

faulting events have occurred along these faults, e.g., 1899 Büyük Menderes, 1928 Torbalı, 1955 Balat, 1969 Alaşehir, 1969 Menderes, 1969 Simav, 1970 Gediz and 1995 Dinar Earthquakes. NW to SE striking normal fault systems mostly takes place in Southwestern Aegean such as Pamukkale, Dinar and Yatagan-Mugla faults.

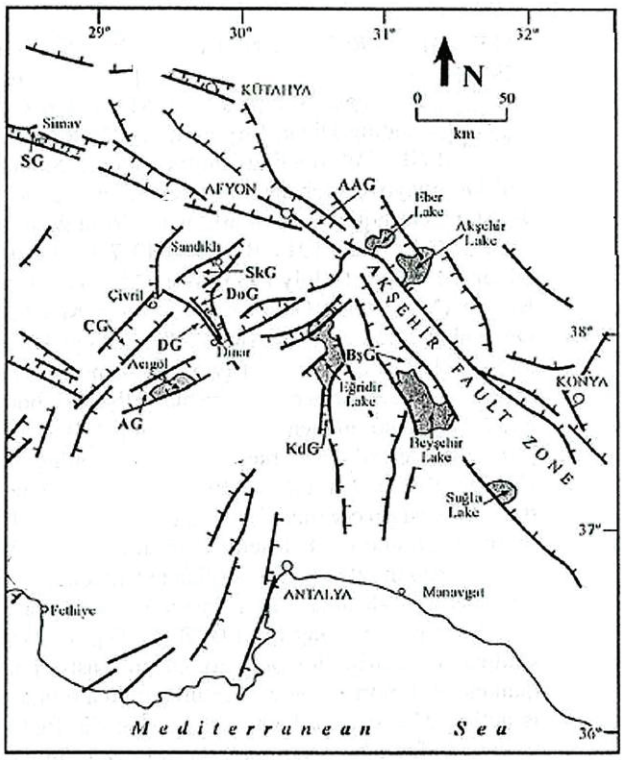

Figure 2.3 Simplifed map showing major structural elements of Isparta Angle and the adjacent areas. Heavy lines with hachures show normal faults: hachures indicate down-thrown side. AG-Acıgöl Graben, CG-Çivril Graben, DG-Dinar Grabcn, SG-Simav Graben, AAG-Akşehir-Afyon Graben, BşG-Beyşehir Graben, DoG-Dombayova Graben, KdG-Kovada Graben, SkG-Sandıklı Graben. (Modified and simplified from Bozkurt, 2001)

One of the main active fault systems in this area is Sultandağı fault (Şengör et al., 1985). The Sultandağı fault is a NW-SE trending fault separating the Sultandağı rise and the Akşehir-Afyon Graben. There have been many suggestions to explain the features and mechanism of Sultandağı Fault. According to Boray et al. (1985), the fault played an important role in the formation of Isparta Triangle and activated as a dextral strike-slip fault during neotectonic era. According to Şaroglu et al. (1987), this dextral strike-slip fault continued its activity as a thrust fault. Barka et al. (1995), also identified the fault as reverse fault. On the other hand, Koçyiğit et al. (2000) name the fault as the "Akşehir fault" and define it as a normal fault with oblique offset and relate the formation of Eber and Akşehir lakes to this fault.

Sultandağı unit (Figure 2.4) comprises rock units, which do not show metamorphism concerning Cambrian-Eocene (Özgül, 1991). Opposite to Sultandağı units, Çay and

Doğanhisar units comprise rock units, which show low graded metamorphism concerning Cambrian-Cretaceous and do not comprise Eocene sediments (Özgül, 1991). Bolkar Mountain unity consists of Paleozoic and Mesozoic metamorphits at the northern part of Taurus Mountains. It tectonically overlie to Geyik Mountain unity which is located at southern part and comprises Sultandağ unit.

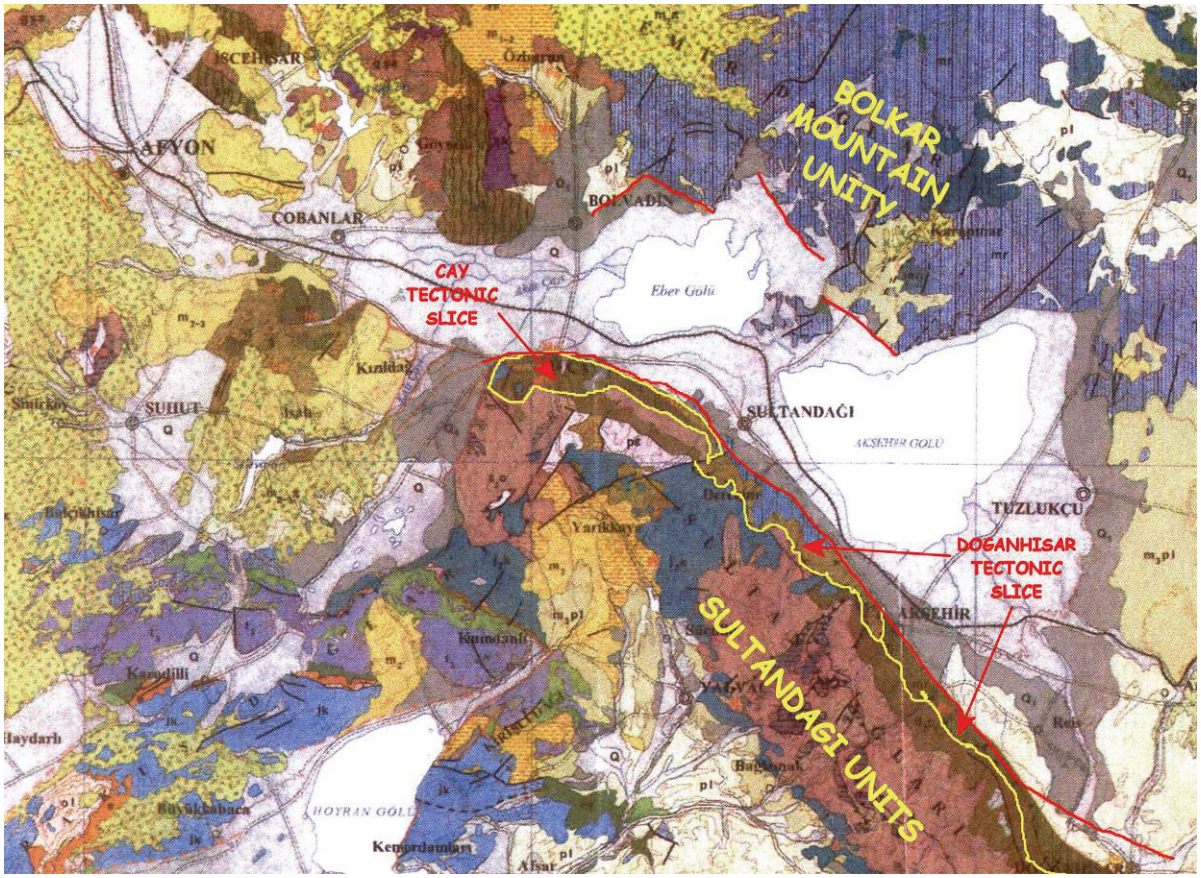

Figure 2.4 Geologic map of Afyon-Sultandağı-Akşehir region (scale: 1:5000) (Modified and simplified from MTA Geology MAP) (See in the text for the explanations)

The Sultandağı fault is a part of a tectonic structure called Isparta Angle which falls into an area where Africa, Central Anatolia and Western Anatolia blocks interact. The Isparta Angle forms the junction between Cyprus and Hellenic arcs bounded by the Sultandağı fault. Barka et al. (1995) reported very little or no motion relative to Eurasia obtained from GPS measurement during 1988-1992 in Isparta Angle in SW Turkey, but in contrary east of Isparta Angle (central Turkey) moves westward relative to Eurasia at about 15 mm/year. The GPS measurements show that the block model which is proposed by Reilinger et al. (2006), has a good fit to the observations overall. As shown in Figure 2.5,

residual motions in western Turkey are large, reaching 7 mm/yr and indicating unmodeled N-S extension. Reilinger et al. (2006) reported that more detailed modeling is warranted in western Anatolia, although beyond the scope of their regional study. In addition, they found an evidence of a small component of trench parallel extension (~ 2 mm/yr) along the leading edge of both the SW and SE Aegean blocks.

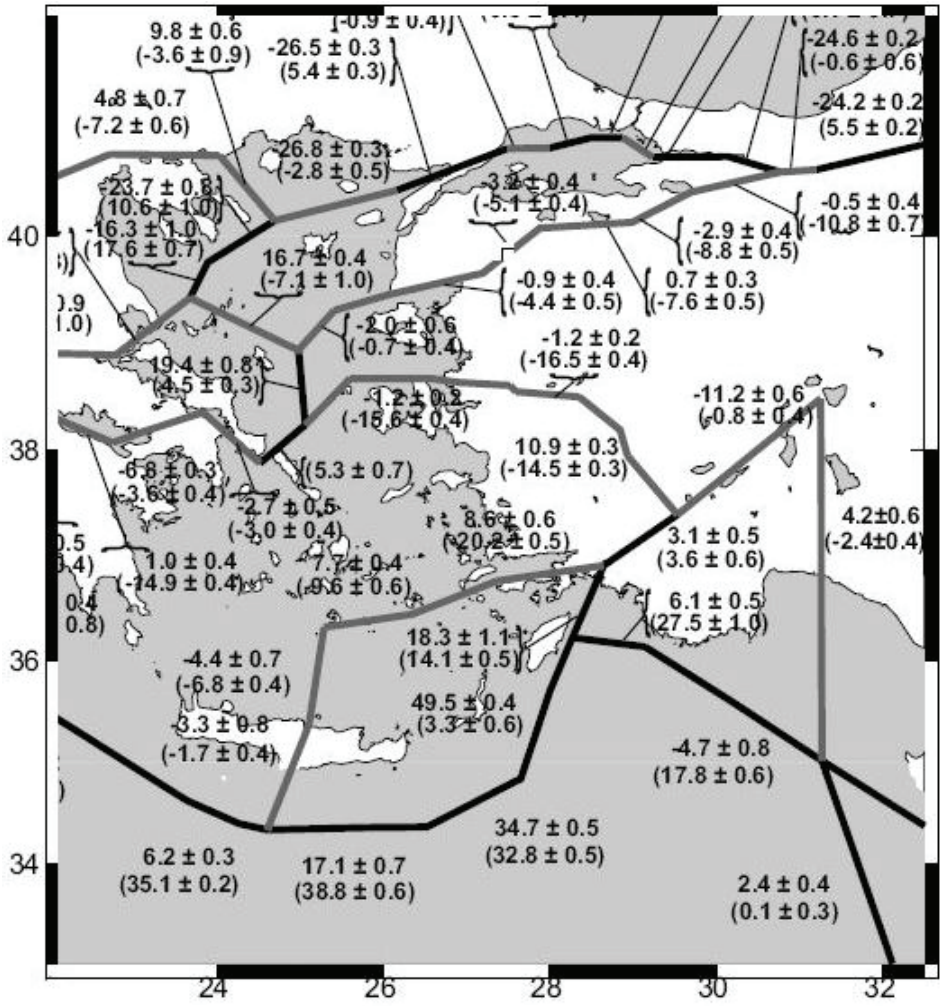

Figure 2.5 Map showing fault slip rates (mm/yr). Upper numbers (no brackets) are strike-slip rates, positive being left-lateral. Numbers in brackets are fault-normal slip rates, positive being closing. (Modified from Reilinger et al., 2006)

3. SEISMICITY

The Aegean Sea, the surrounding Greek coasts and the western Turkey, along with the Hellenic Arc, are the most active seismic areas of the Mediterranean Basin and of the whole Alpine-Himalayan chain. The catalogues of seismicity are certainly incomplete for low magnitude events (M<4), but the map permits to identify the active seismogenic zones in a broad scale. Several earthquakes with magnitudes greater than 6 occurred during the instrumental period. The seismicity distribution shown in Figure 3.1 and the trend of the focal mechanisms in Figure 3.2 are related to the major tectonic features. The earthquake depths are generally normal (<15 km), with exception for the subduction zones where the events occur at intermediate and high depths (>30 km). This happens along the Hellenic Arc and in the Antalya Gulf (southern Turkey). In the whole area, the frequency of events with magnitude greater than 4, is evident, but there are many events with lower magnitudes.

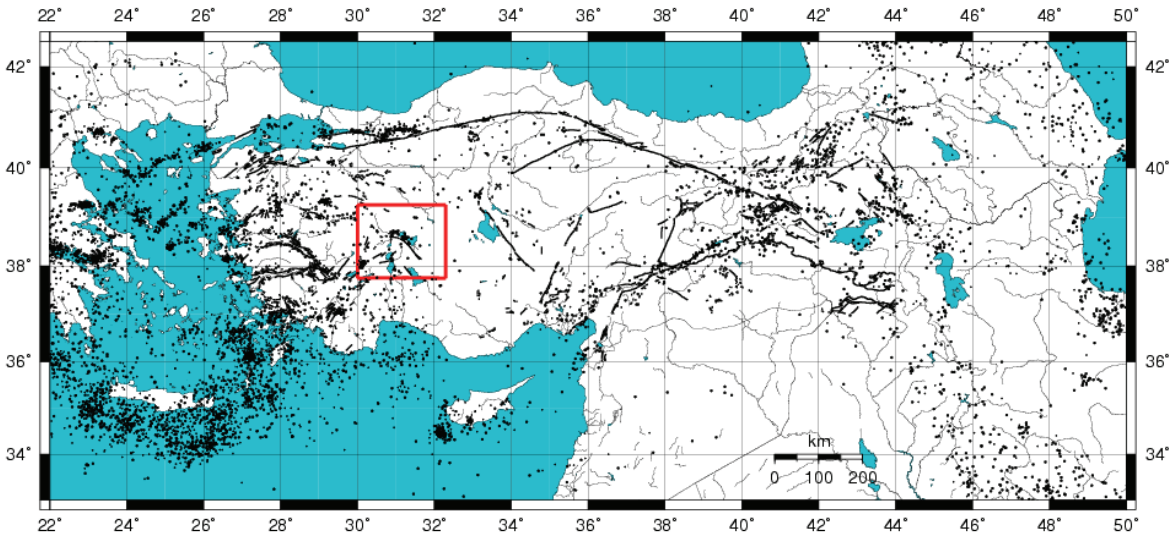

Figure 3.1 Seismicity of the eastern Mediterranean region for the period of 1975-2006 with magnitudes, greater than 4 (NEIC Catalog).

The moment tensor solutions of earthquakes with magnitudes greater than 5.0 between 1955 and 2000 in the region are shown in Figure 3.2 (Kiratzi and Louvari, 2003).

It is well known that large historical earthquakes have repeatedly affected the Burdur-Dinar region. Records of this century indicate in Burdur (37.50N, 32.50E) 3 October 1914 (M 7) earthquake, where about 4000 people died and about 17000 houses destroyed, about 100 houses were destroyed in the villages between Bolvadin and Çay. Another earthquake of magnitude 6.0 occurred on 7 August 1925 in Afyon-Dinar causing damage in the region lying between Hamidiye and Denizli. On 12 May 1971, an earthquake of magnitude 6.2 occurred in the town of Burdur destroying 1487 houses and killing 57 persons. Another earthquake of magnitude 6.1 occurred on 1 October 1995 causing extensive damage in Dinar. The earthquake killed 90 people with 260 injured and caused extensive damage to 30% of buildings in Dinar.

The Sultandağı fault with a clear topographic imprint has been relatively free of the historical earthquakes. The fault was recently activated by 15 December 2000 (M_w=6.0) Bolvadin earthquake (S-1), which occurred in the southeastern part of the fault zone. The earthquake caused 6 casualties with 82 injuries and caused damage in Bolvadin, Akşehir and Ilgın provinces. On 3 February 2002, another earthquake with magnitude M_w=6.5 (S-2) occurred on the northwestern part of the Sultandağı fault.

3.1. Relocation Processes

S-1, S-2 and aftershock activities related to the Sultandağı fault revealed the true nature of the faulting. However due to the poor station coverage in the region there were inconsistencies on the location of the mainshocks reported by a number of agencies. Table 3.1 presents a summary of the locations by different agencies. Figure 3.3 shows that the locations reported by KOERI and USGS are not occurring on the Sultandağı fault but on the northeast of the topographic imprint delineating the fault. In addition, S-2 event was located on the south of S-1 by KOERI, which presents an obvious difficulty of constructing fault geometry.

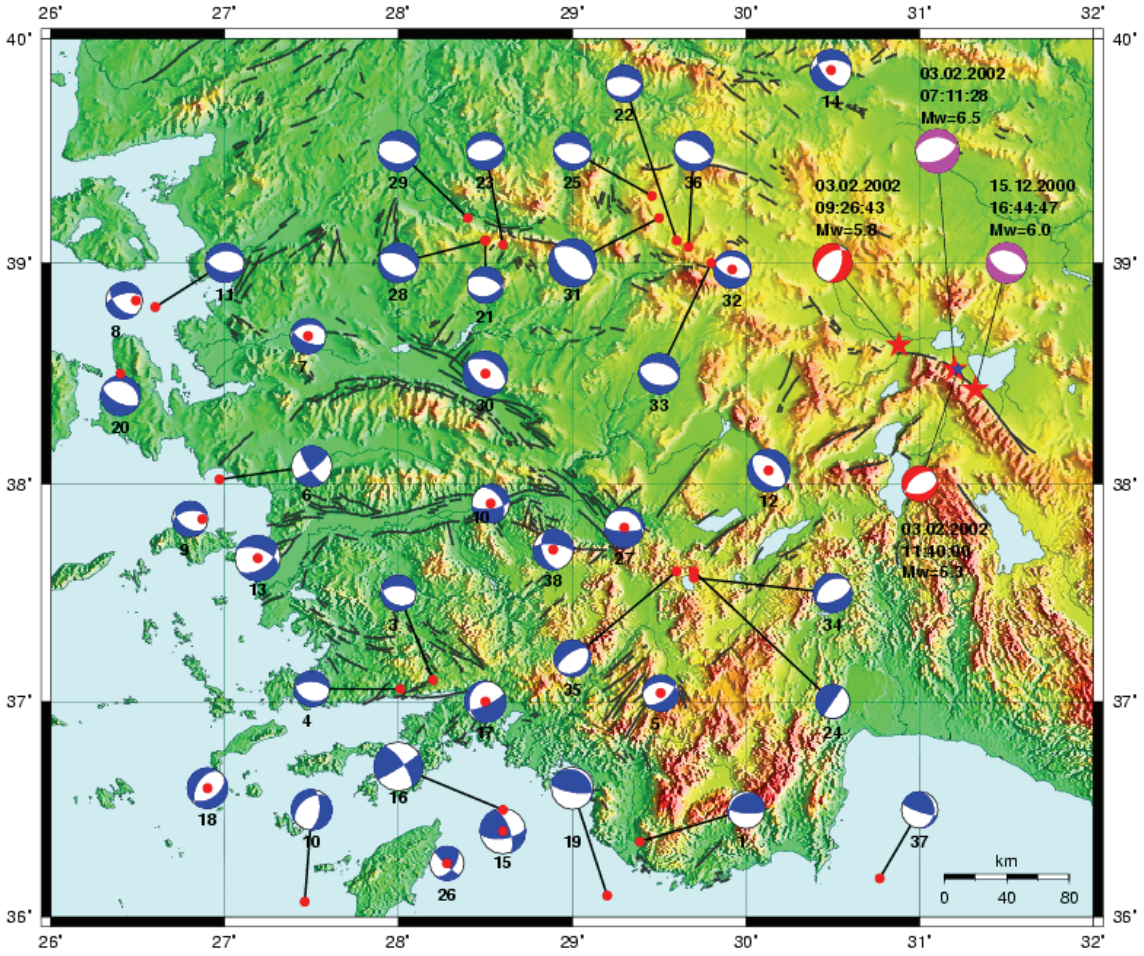

Figure 3.2 Focal mechanism of events between 1955-2000 and the major after shocks (from Kiratzi Louvari, 2003). Event properties and focal mechanisms are given in Appendix 2. The recent earthquakes are also shown (red balls).

Table 3-1 Locations of S-1 and S-2 determined by different agencies.

Event	*Agency*	*KOERI*	*USGS*	HARVARD	ISC	This Study
S-1	***Latitude***	38,590	38,457	38,400	38,402	38,43
	Longitude	31,160	31,351	31,350	31,325	31,32
	Depth	5,8	7,0	15,0	10,0	-
S-2	***Latitude***	38,580	38,573	38,620	38,520	38,52
	Longitude	31,250	31,271	31,210	31,200	31,20
	Depth	10,0	22,0	15,0	22,1	-
S-3	***Latitude***	38,68	38,632	38,23	38,63	38,667
	Longitude	30,84	30,902	30,56	30,88	30,856
	Depth	10,0	15,0	15,0	24,9	-

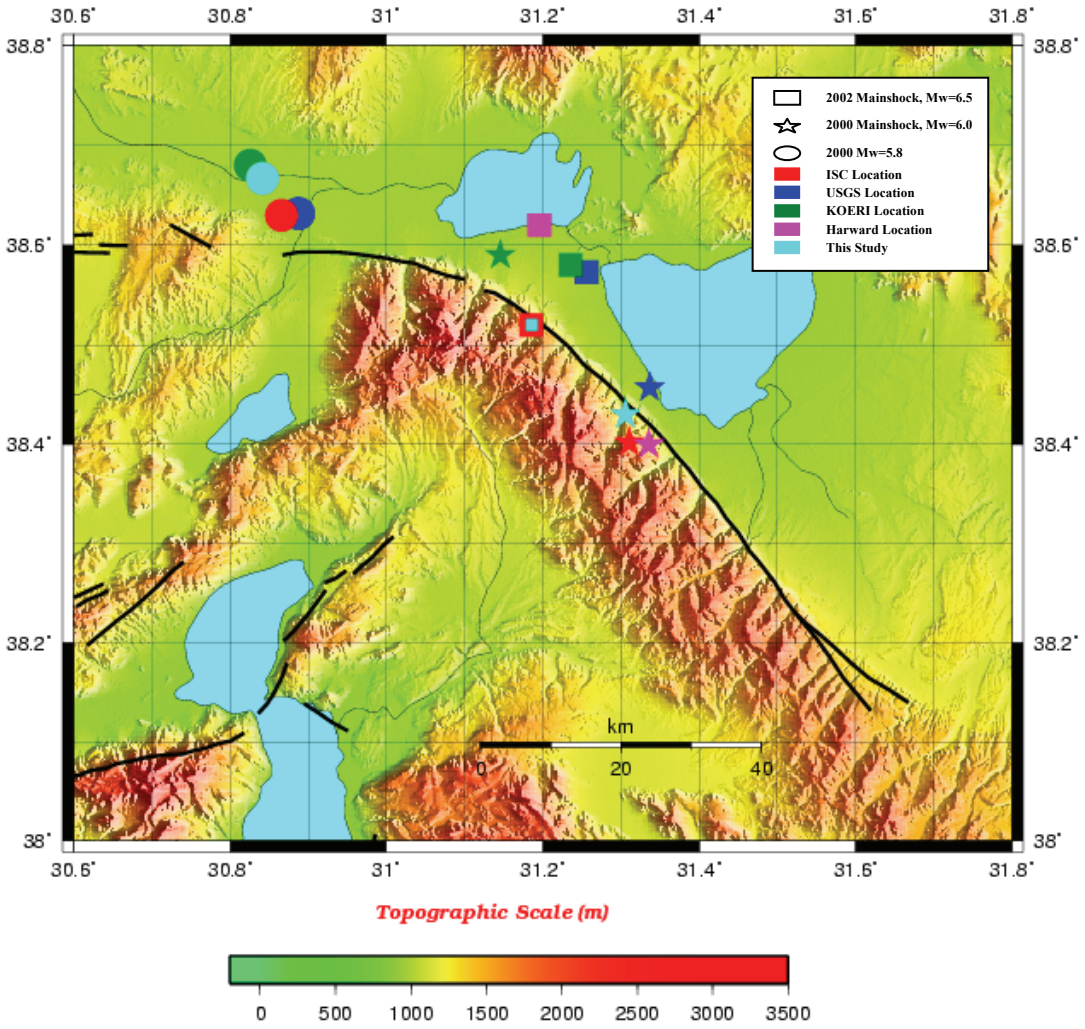

Figure 3.3 Locations of the S-1, S-2 and S-3 plotted on a topographic map. Square, star and circle symbols are used to show locations of S-1, S-2 and S-3 respectively.

3.1.1. Relative Location of Two Mainshocks

The locations of two mainshocks had large uncertainties due to poor station coverage. As a result, we employed a relative location technique (Gutenberg sine-curve method)(Wyss and Brune, 1967). Taking the ISC location of S-2 as the master event, S-1 was located relatively using the P-wave arrival time differences to stations, which recorded the mainshocks within a 2000 km distance range. The stations, which are used in relative location test, are shown in Figure 3.4.

If we assume that both events have similar depths, (Harvard reported that both events have same depths), the relative time differences (dt) between events are expected to follow a sine curve when plotted as a function of the azimuth of the stations. Time difference is given by,

$$dt = (T_1 - OT_1) - (T_2 - OT_2), \qquad 3.1$$

OT_1 = Origin Time of the Master Event

OT_2 = Origin Time of the other Event

T_1 = P-arrival time of Master Event to the station

T_2 = P-arrival time of other Event to the station

dt = P-arrival time difference.

The reliability of the results will depend on the assumptions. If the depths of two events are significantly different, this will introduce errors in the final estimate. Another source of error is related to the assumption that Pn velocity is constant for each source-receiver pair. Significant deviations from the average Pn velocity (8.0 km/s) may bias the estimated sine curve. It is obvious that we assumed the location of the master event is correct. We did not attempt to improve the location of the master event.

The azimuthal variations of the P-arrival time differences are shown in Figure 3.4 for the earthquake pair, together with the sine curve. As a result, we estimated that the distance between two earthquakes is approximately 16 km and S-1 is at an azimuth of 135° with respect to S-2. As shown in Figure 3.4, the result is in agreement with the location presented by ISC.

3.1.2. Relocation of the aftershocks

In order to study the details of the rupture geometry and estimate the seismic moment, it is necessary to have an accurate distribution of the seismicity. However, poor station coverage and low quality of waveform data limit our ability on the accuracy. We used the existing waveform data to relocate large aftershocks of the two mainshocks. Figure 3.5 shows the permanent seismic stations used in this study operated by KOERI and TÜBİTAK-MRC. The stations with the exception of ISP have single component sensors

with sampling rate of 20 Hz. The distance of the activity to the nearest station is greater than 100 km making it difficult to pick accurately the first arrivals. The reading of S phases was not possible on the vertical components.

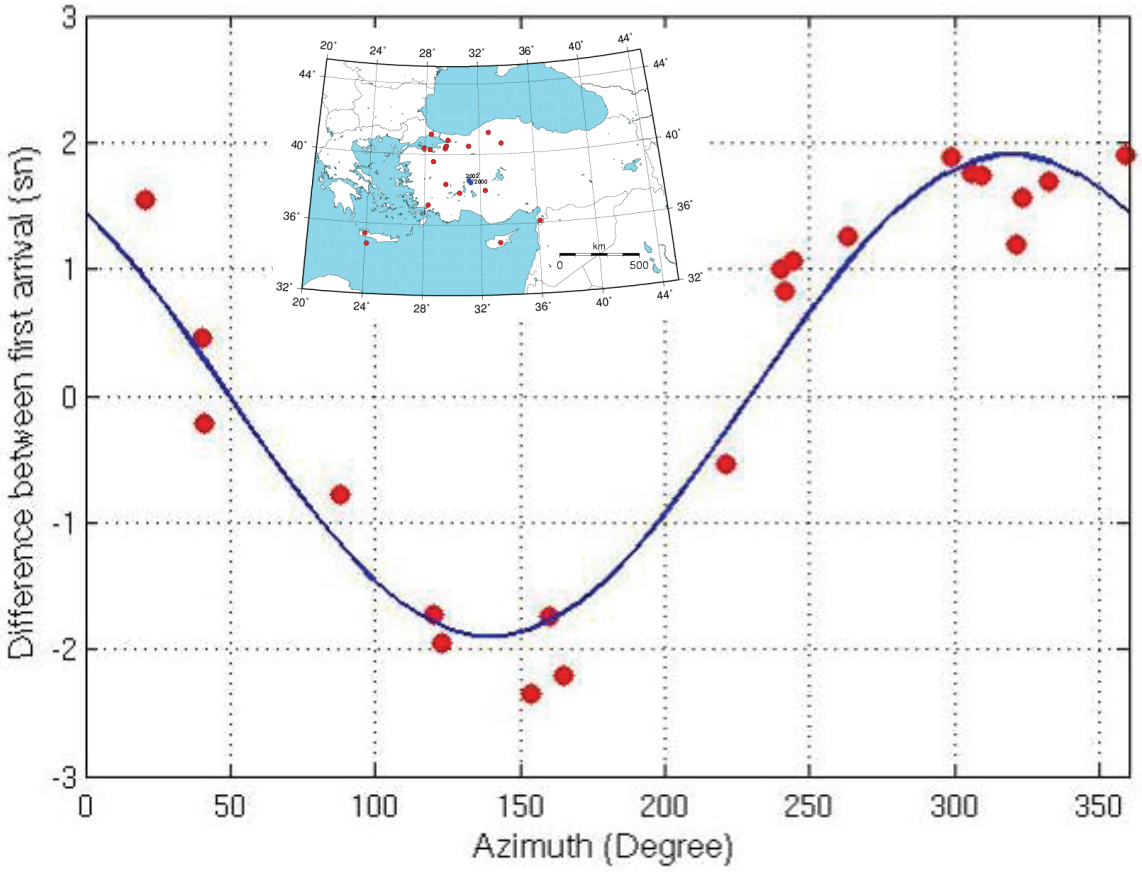

Figure 3.4 The azimuthal variations of the P-arrival time differences. The map shows the station locations.

In order to reduce the uncertainties on the picks of the P arrivals we used cross correlations to search waveform similarity between the preselected waveforms recorded well by the stations and the rest of the catalog. The large correlation values provided events with similar waveforms. Knowing the P arrival time of the reference waveform, we associated phases such as Pg and the largest S phase in the coda to align the waveforms. This improved the picks of the P wave arrival times. We then located the aftershocks using HYPO71 (Lee and Lahr, 1975). Since the number of the stations and the azimuthal distribution were not sufficient to use VELEST (Kissling et al., 1994), we constructed a velocity model manually by reducing the rms errors on the locations (Figure 3.6).

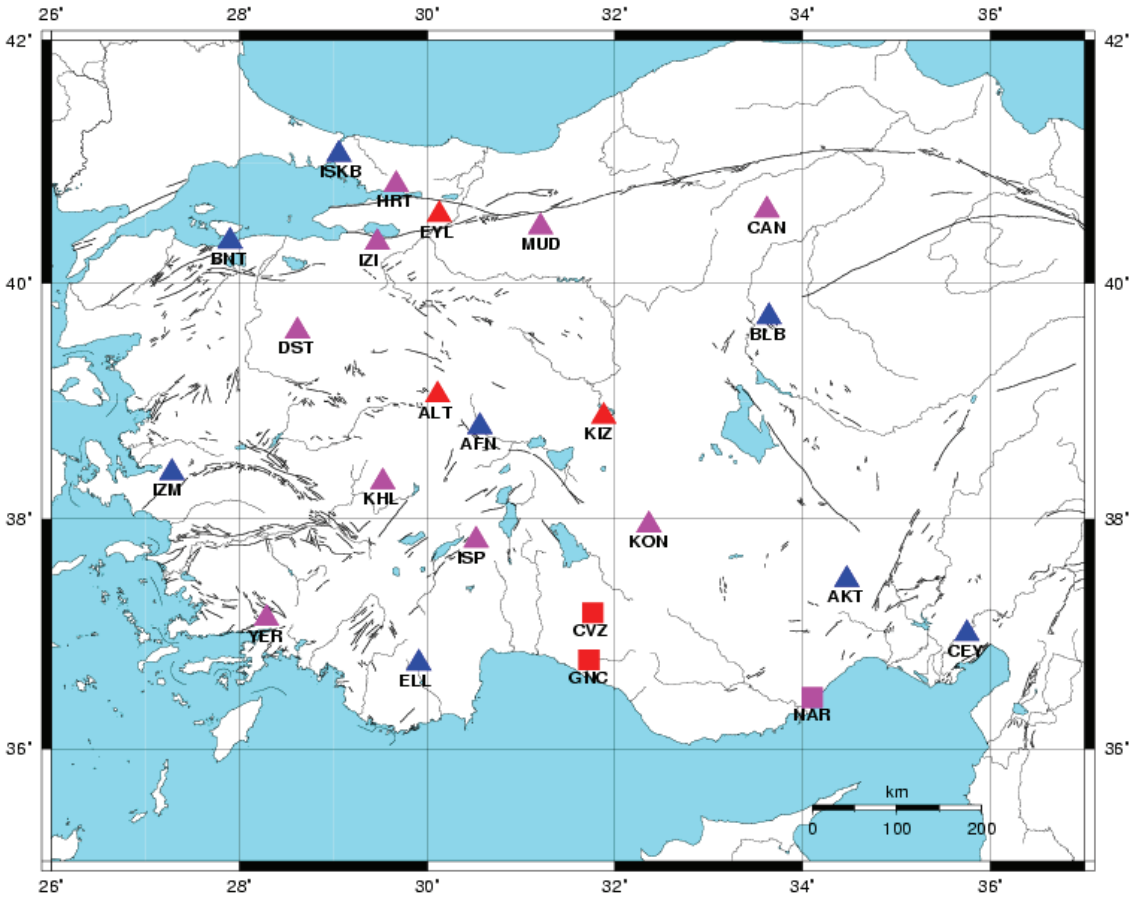

Figure 3.5 Location of the KOERI (triangles) and TÜBİTAK-MRC (squares) stations used for locating S-1 and S-2. Red: only used for S-1, Blue: only used for S-2 and Purple: used for both S-1 and S-2.

A total of 140 aftershocks were relocated using the technique above and illustrated in Figure 3.7-3.8 The average horizontal errors estimated by the HYPO71 were less than 4.0 km N-S and 4.0 km E-W, respectively. The depths are not well resolved due to the lack of S phases and close stations.

The aftershock locations of S-1 (Figure 3.7) show that the rupture started in the middle of the fault and propagated bilaterally. The length of the rupture is approximately 25 km consistent with the moment magnitude estimate assuming 20 cm of slip. It is interesting to observe that another cluster on the northwestern extremity of the fault started approximately three months after the main shock. The distance between the mainshock of S-1 and the activity is greater than 40 km.

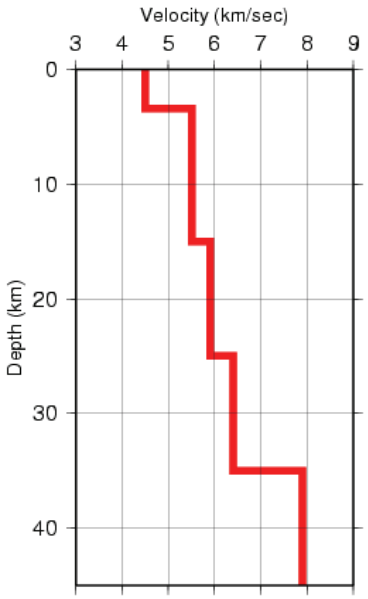

Depth (km)	Velocity (km/sec)
0,00	4,50
3,40	5,51
15,00	5,90
25,00	6,40
35,00	7,90
45,00	8,10

Figure 3.6 The velocity model used in this study.

Similar analysis was performed on the aftershock sequence of S-2. Figure 3.8 shows the distribution seismicity of the first one-week following the mainshock. The inaccuracies on the locations prevent constraining the fault geometry and estimating the seismogenic zone accurately. However, it is still observed that the rupture propagated to the northwest on the continuation of S-1. A high resolution seismicity was obtained by TÜBİTAK-MRC from an aftershock study after one week following the mainshock using a local network (Figure 3.9). The study provided a better estimate of the seismic moment and the rupture geometry.

The length of the rupture is estimated as 40 km from the seismicity, which is in agreement with the moment magnitude of 6.5 with a slip of 35 cm. The rupture approximately started at the termination of S-1 and propagated to the northwestern termination of the fault. We also observe an activity at the termination of S-2 rupture similar to one during S-1 rupture. S-3 occurred in the area about 2 hours after the mainshock with a focal mechanism of different orientation.

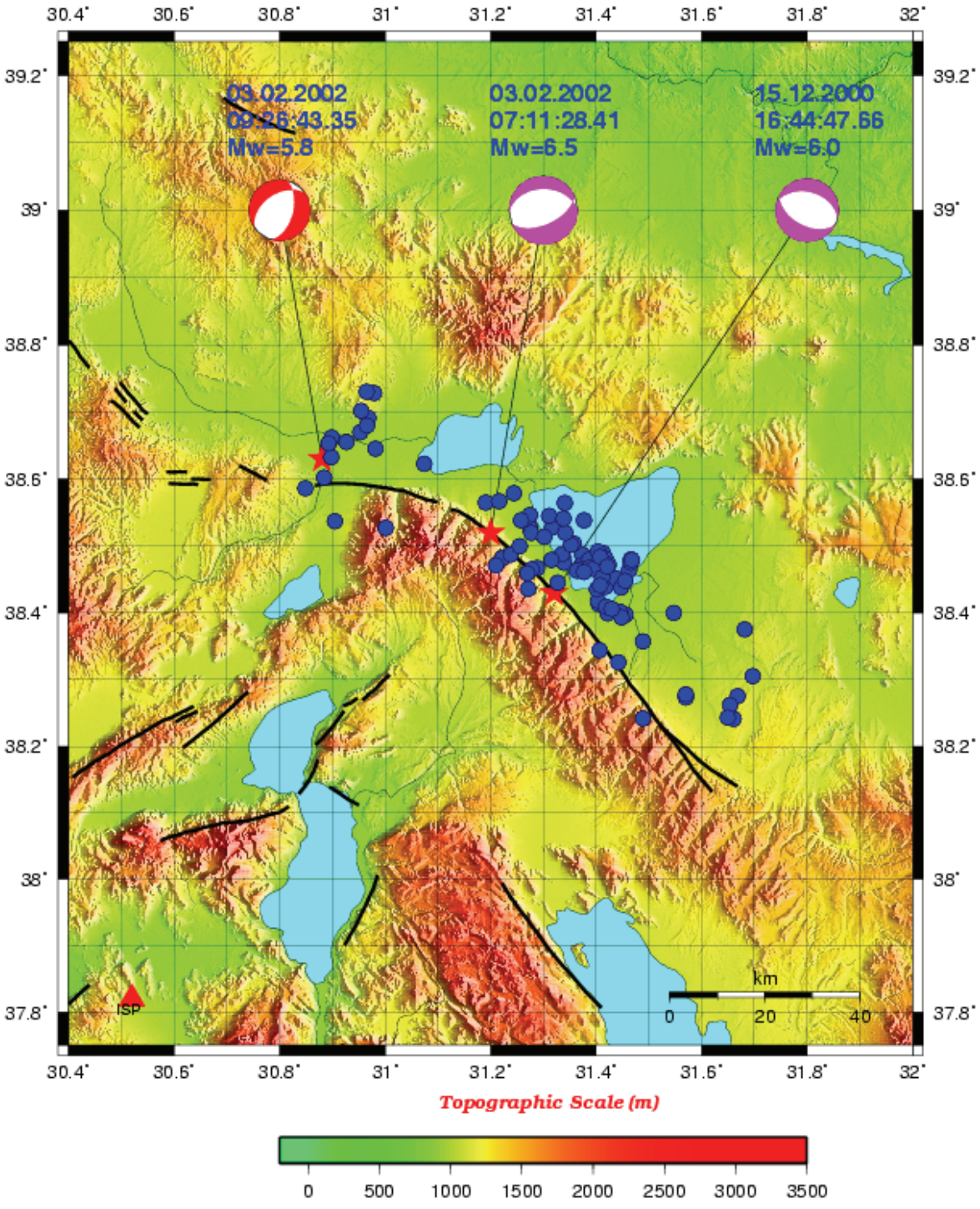

Figure 3.7 Map view of the relocated events with magnitudes greater than 3.5 following S-1 for 7 months period. Red stars show 3 mainshocks.

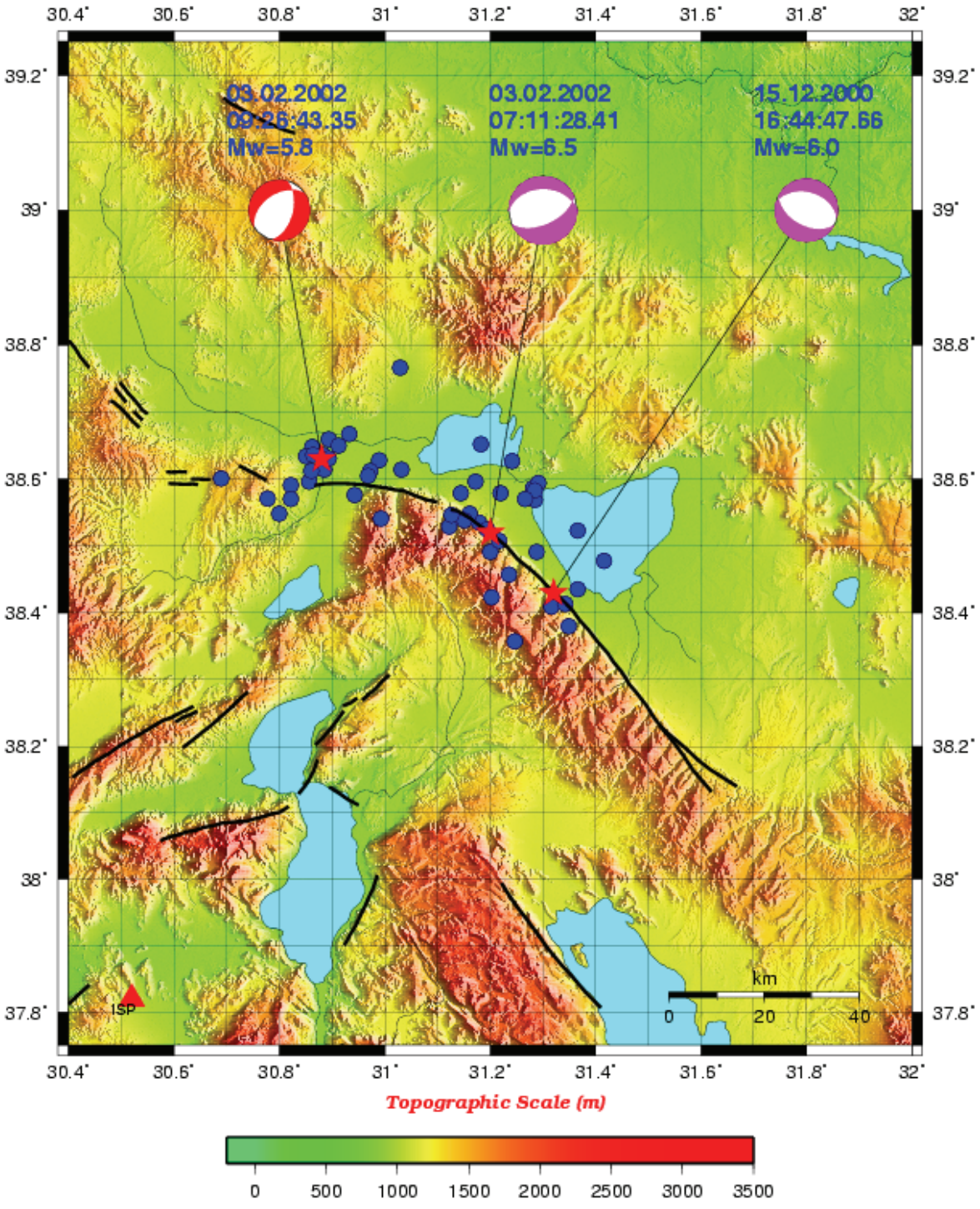

Figure 3.8 Map view and depth section of the relocated events with magnitudes greater than 3.5 following S-2 for 7 days period. Red stars show 3 mainshocks.

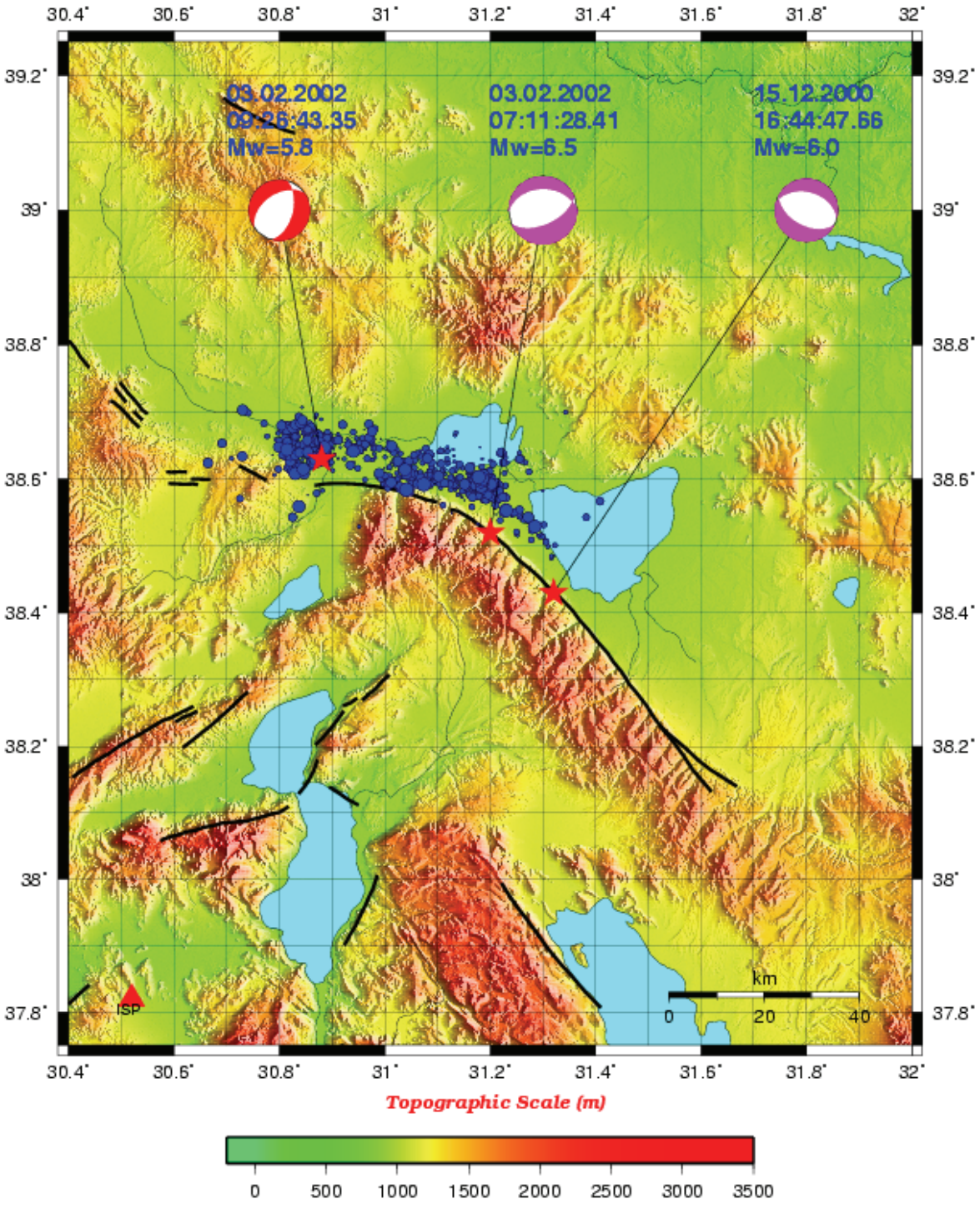

Figure 3.9 Map view and depth section of the relocated events by TÜBİTAK-MRC following S-2 event. The network was installed one week after the mainshock and recorded one week. Red stars show 3 mainshocks.

3.2. Rupture Directivity

Two earthquakes on the same fault occurring approximately 2 years apart have interesting seismological implications. It is important to understand how much S-2 brought the northern segment of the fault closer to the failure. The interactions between two earthquakes require knowledge of the slip distribution and rupture parameters. Although the relocation of the mainshocks and the aftershocks indicate that both events propagated dominantly to the northwest we would like to test this hypothesis further using forward modeling of the waveforms recorded by the nearest broadband station. The ISP station is approximately 100 km away from the two earthquakes at an azimuth of 90 degree to the Sultandağı fault (Figure 3.7-3.9). As a result, the effect of the distance of two earthquakes to the station is relatively minor. It is worth to explore the possibility that the waveforms of two events might be sensitive to the rupture directions. Figure 3.10 and 3.11 show 3 component velocity recordings of two events. Although two earthquakes occurred at similar azimuths with respect to the station and have similar distances from the station the waveforms are quite different.

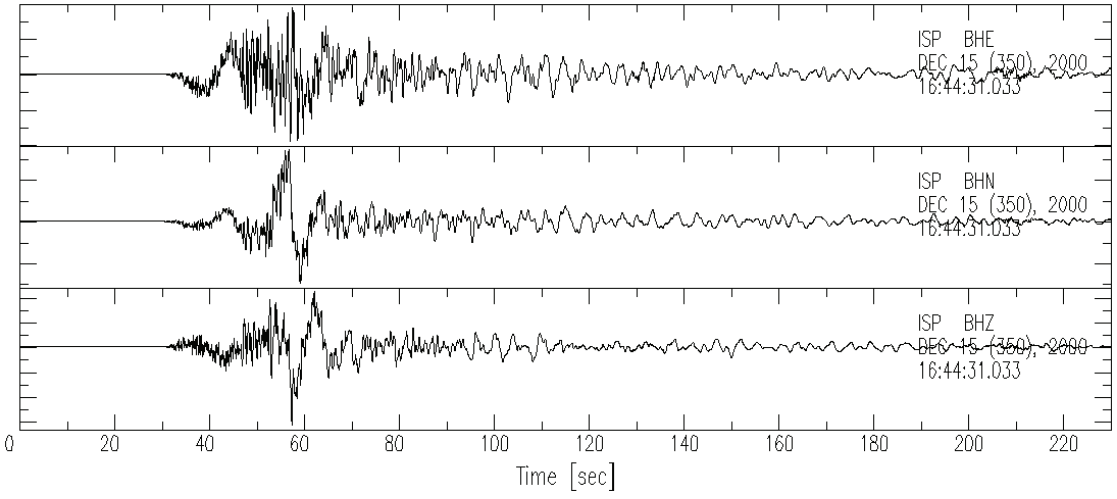

Figure 3.10 Three component velocity waveforms of S-1.

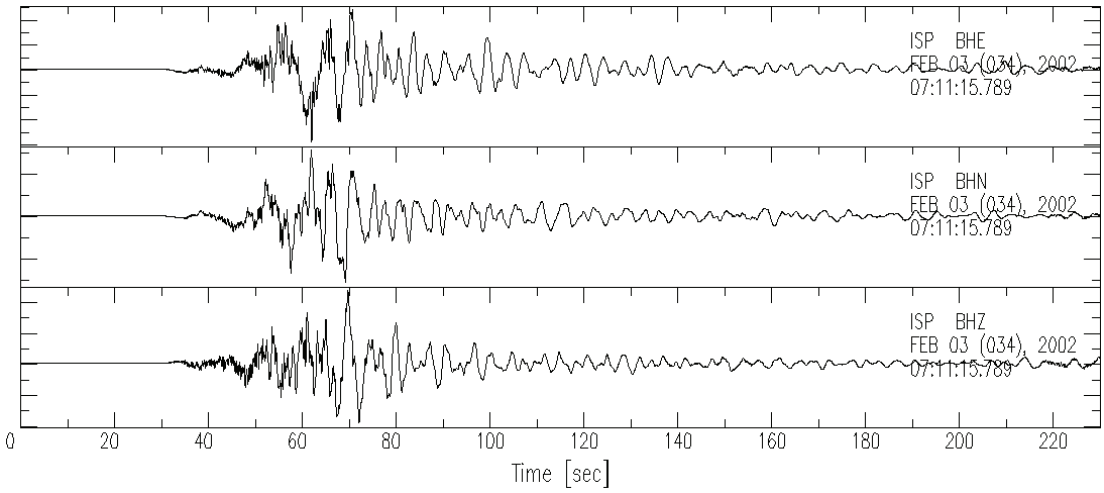

Figure 3.11 Three component velocity waveforms of S-2 recorded at ISP station.

We used discrete wave number method (Bouchon, 1982) to compute synthetic waveforms. We integrated the velocity seismograms to obtain displacements. The parameters for the source mechanisms presented on Table 3.2 and we used the same velocity model (Figure 3.7) that is used in the relocation processes. We assumed constant slips, 20 cm and 35 cm, for both earthquakes and a rupture velocity of 2.7 km/sec. We changed the location of the epicenter with respect to the fault boundaries starting at the beginning of the fault (northern extremity) increasing with 5 km intervals. Figures 3.12-3.13 show the computed waveforms for different epicenter locations and the observed displacement waveforms. The results indicate that although epicenter of S-1 can be placed on between 15-25 km and epicenter of S2 can be placed on 20-40 km from the northwest extremity of the faults, the both ruptures almost propagated dominantly to the northwest. This is consistent with the aftershock distributions and the locations of the mainshocks obtained in this study.

Table 3-2 Source mechanisms of S-1 and S-2.

Earthquake	***Strike***	***Dip***	***Rake***	**Depth**	**Magnitude (M_w)**
S-1	*285*	41	100	8.0	6.0
S-2	*269*	37	71	8.0	6.5

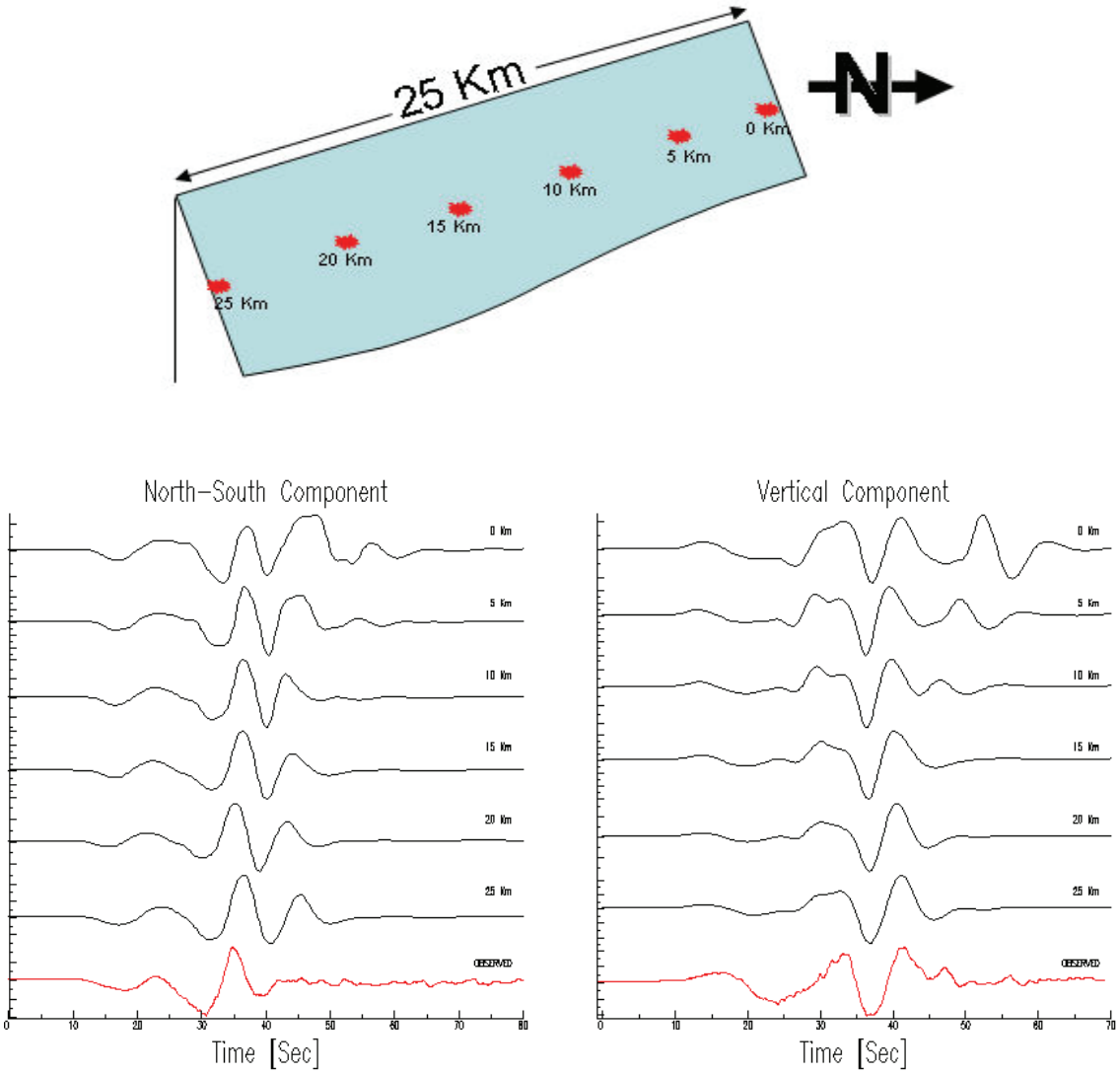

Figure 3.12 Computed waveforms for different epicenter locations. The red trace on the bottom shows observed displacement for S-1 event at ISP station.

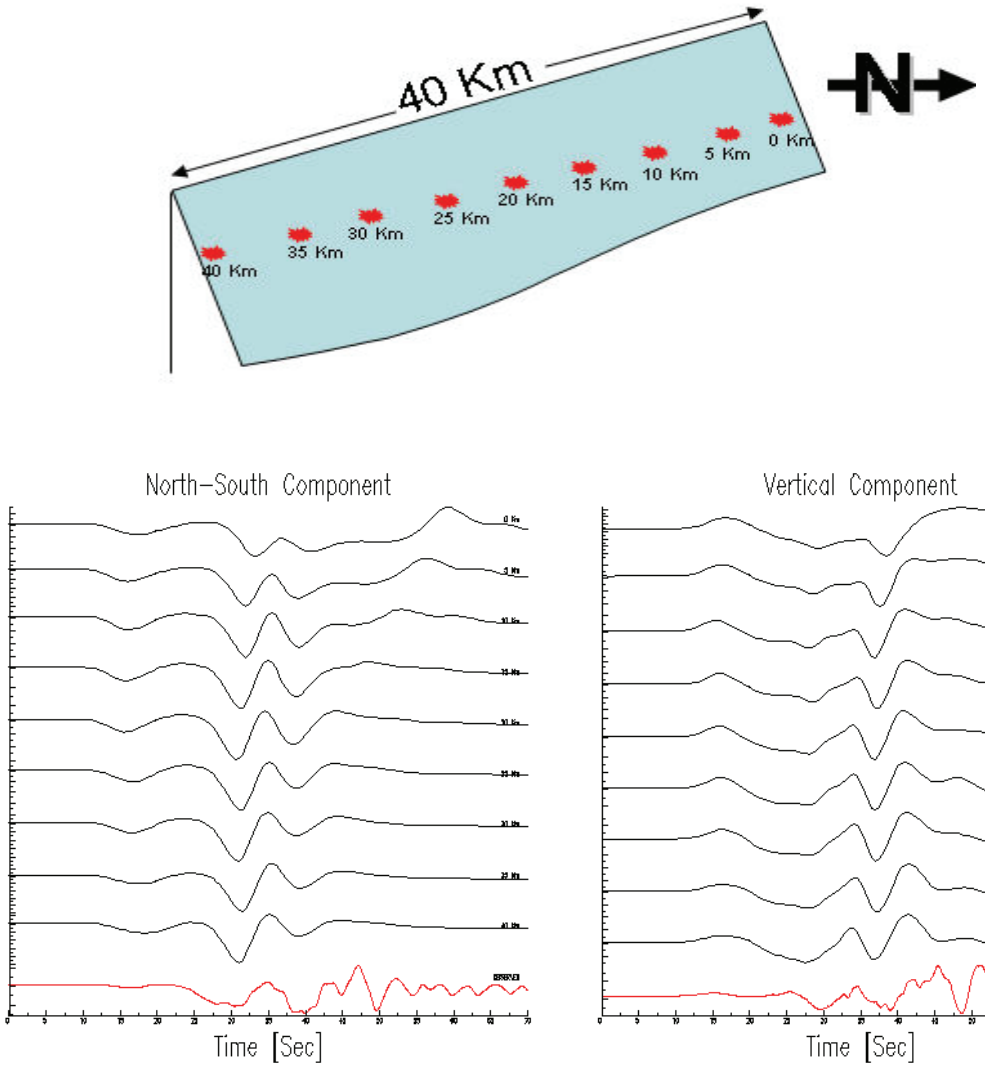

Figure 3.13 Computed waveforms for different epicenter locations. The red trace on the bottom shows observed displacement for S-2 event at ISP station.

4. COULOMB STRESS MODELING APPROACH

4.1. Stress

The fundamental dynamic and kinematic quantities of rheology are stress and strain, respectively. Let a point P in a continuous medium occupying a volume V in Cartesian space, and ΔV be an element of volume inside it. This volume element is acted upon by two kinds of forces, i.e. body forces, per unit volume and surface forces acting on the surface ΔS bounding ΔV. The traction vector on the surface (ΔS) of the continuum at the point P is defined as,

$$T(n) = \lim_{\Delta S \to 0} \frac{\Delta F}{\Delta S} = T_1 \hat{x}_1 + T_2 \hat{x}_2 + T_3 \hat{x}_3 \qquad \textbf{4. 1}$$

That represents the force per unit are acting on the surface with orientation specified by the normal vector. It can be specified Pa or bar (1 bar = 0.1 MPa = 10^6 dyn/cm^2). If the equation above generalizes,

$$\sigma_{ij} = \lim_{\Delta S_i \to 0} \frac{\Delta F_j}{\Delta S_i} \qquad \textbf{\textit{i, j = x, y, z}} \qquad \textbf{4. 2}$$

Stress is a second order tensor which represents the state of stress throughout the volume. The tensor represents complete internal force distribution at any surface, which intersects the volume at P. The first index of σ_{ij} corresponds to the direction of the normal to the plane being acted on by the force, and the second index indicates the direction of the force.

$$\sigma_{ij} = \begin{pmatrix} \sigma_{xx} & \tau_{xy} & \tau_{xz} \\ \tau_{yx} & \sigma_{yy} & \tau_{yz} \\ \tau_{zx} & \tau_{zy} & \sigma_{zz} \end{pmatrix} \qquad \textbf{4. 3}$$

where the diagonal terms (σ_{ii}) are called normal stress and the off-diagonal terms ($\tau_{ij} = \tau_{ji}$) are called shear stresses acting on ΔS. Due to the symmetry ($\tau_{ij} = \tau_{ji}$) the stress tensor has 6 independent components. Normal stress with positive value is called tensional stress and negative value is called compressional stress. The state of stress at depth in the earth is always compressional. The normal stresses are defined as principle (compressive) stresses, where the maximum principle stress (which has a greatest absolute value of normal stress)

is σ1 and minimum principle stress (which has a smallest absolute value of normal stress) is σ3.

4.2. Coulomb Failure

Coulomb Failure Criterion is widely used to characterize the conditions under which failure occurs in rocks. In the Coulomb criterion, failure occurs on a plane when the Coulomb stress σ_f exceeds a specific value

$$\sigma_f = \tau_\beta - \mu(\sigma_n - p) \qquad \textbf{4. 4}$$

where τ_β is the shear stress on the failure plane, σ_n is the normal stress, p is the pore fluid pressure and μ is the coefficient of friction. (King et al., 1994, Hodgkinson et al., 1996, Harris, 1998).

In this equation τ_β must be positive for the right lateral shear stress and σ_n must be positive for the compression. The normal and shear stress acting on the failure plain can be expressed in terms of the principal stresses (Jaeger and Cook, 1979);

$$\sigma_n = \frac{1}{2}(\sigma_1 + \sigma_2) - \frac{1}{2}(\sigma_1 - \sigma_3)\cos 2\beta \qquad \textbf{4. 5}$$

$$\tau_\beta = \frac{1}{2}(\sigma_1 - \sigma_3)\sin 2\beta \qquad \textbf{4. 6}$$

where σ_1 is the greatest principal stress and σ_3 is the least principal stress.

Then σ_f equation becomes,

$$\sigma_f = \frac{1}{2}(\sigma_1 - \sigma_3)\sin 2\beta - \mu\left[\frac{1}{2}(\sigma_1 + \sigma_3) - \frac{1}{2}(\sigma_1 - \sigma_3)\cos 2\beta - p\right] \qquad \textbf{4. 7}$$

and by differentiating equation as a function of β, one finds that the maximum coulomb stress occurs when

$$\cot 2\beta = -\frac{1}{\mu}. \qquad \textbf{4.8}$$

Increasing the pore pressure (i.e. positive values) causes decreasing the normal stress. When rock stress is changed more rapidly than fluid pressure can change through flow, p can be related to confining stress in the rock by Skemptons coefficient B, where B varies between 0 and 1. If the effective coefficient of friction is defined by

$$\mu' = \mu(1 - B). \qquad \textbf{4. 9}$$

Equation becomes

$$\sigma_f = \tau_\beta - \mu' \sigma_n \qquad \textbf{4. 10}$$

In coulomb stress modeling part, this equation is used.

4.3. Change Of Coulomb Stress On Faults Of Specified Orientation

X, Y axes and fault displacements are horizontal, and fault planes are vertical. Stresses on a plane at an angle ψ from the x axis (Figure 4.1) is given by,

$$\sigma_{11} = \sigma_{xx} \cos^2 \psi + 2\sigma_{xy} \sin\psi \cos\psi + \sigma_{yy} \sin^2 \psi \qquad \textbf{4. 11}$$

$$\sigma_{33} = \sigma_{xx} \sin^2 \psi - 2\sigma_{xy} \sin\psi \cos\psi + \sigma_{yy} \cos^2 \psi \qquad \textbf{4. 12}$$

$$\tau_{13} = \frac{1}{2}\left(\sigma_{yy} - \sigma_{xx}\right)\sin 2\psi + \tau_{xy} \cos 2\psi \qquad \textbf{4. 13}$$

σ_{11}, σ_{33} and τ_{13} denote the stress components in the rotated system.

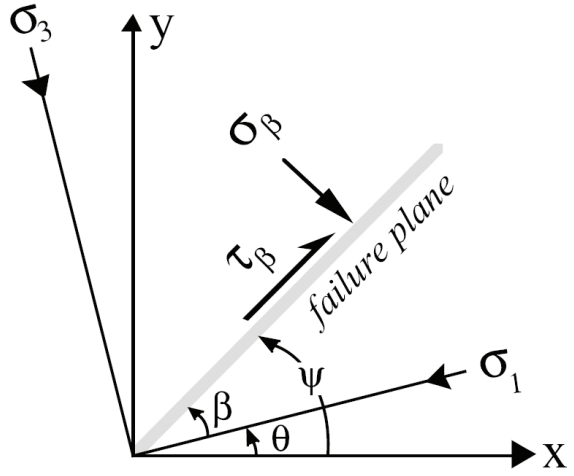

Figure 4.1 The axis system used for calculation of Coulomb stresses on optimum failure planes. Compression and right-lateral shear stress on the failure plane are taken as positive. The sign of τ_β is reversed for calculations of right lateral Coulomb failure on specified failure planes. (King at all, 1994)

Now it can be written as the change of Coulomb stress for the right and the left lateral motion on planes oriented at ψ with respect to the x-axis,

$$\sigma_f^R = \tau_{13}^R + \mu' \sigma_{33} \qquad \textbf{4. 14}$$

$$\sigma_f^L = \tau_{13}^L + \mu' \sigma_{33} \qquad \textbf{4. 15}$$

The results of the Equation 4.14 is illustrated on figure 4.3.a, which outlines shear, normal stress and the Coulomb stress change only induced by constant slip from a master fault. The calculations applied on a rectangular fault in a homogeneous, isotropic, stress-free and elastic medium (Figure 4.2). The shear and normal components contributing to the failure and the resulting Coulomb stress is shown on different panels. The results are appropriate only to determine the effect of the master fault on a nearby fault with the same orientation.

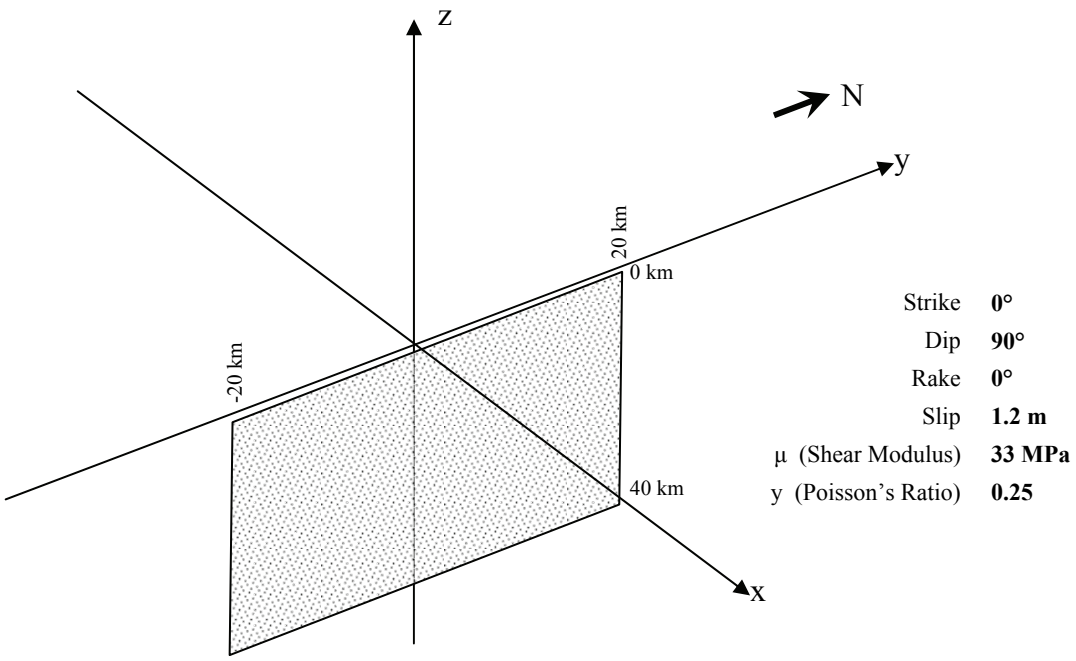

Figure 4.2 Sketch and Parameters for the sample fault model

The results are independent of any knowledge of regional stresses or any preexisting stress fields from other events (King et al., 1994). The red colors in Figure 4.3.a represent an increase of shear stress on the fault. The blue colors show the reduction of this tendency. The important thing is that this situation reverses for the left-lateral slip. The lobes of increased shear stress are located at the fault ends, corresponding to the stress distribution that tends to extend to fault. Off-fault lobes also appear, separated from the fault by a region where the Coulomb stresses have not been increased, as discussed by Das and Scholz (1983) (King et al., 1994).

4.4. Change of Coulomb Stress on Optimally Oriented Faults

The Coulomb stress change produced by a master fault is calculated for a small receiver faults parallel to master fault using the equations. However the change of Coulomb stress should be calculated on optimally oriented faults, which are the planes on which aftershocks might be occur (King et al., 1994).

Because the total stress σ_{ij}^{T} causes to failure consists of the stress produced by an earthquake σ_{ij}^{E} and the regional stress σ_{ij}^{R}. It can be said that regional stress is the result of the tectonic movements in the region. The total stress is,

$$\sigma_{ij}^{T} = \sigma_{ij}^{R} + \sigma_{ij}^{E} . \qquad \textbf{4. 16}$$

The regional stress field is thought to be the result of the given tectonic situation. It is often implemented as simple uniaxial compression (King et al., 1994; Hubert-Ferrari et al., 2000; Parsons et al., 2000; Stein and Hanks, 1998; Pinar et al., 2001). The orientation of the principle axis is calculated from,

$$\theta = \frac{1}{2}\arctan\left(\frac{2\sigma_{xy}^{t}}{\sigma_{xx}^{t} - \sigma_{yy}^{t}}\right). \qquad \textbf{4. 17}$$

θ is the angle (Figure 4.1) between the x axis and the principle axis. The other principle axis can be found by θ+90º. The greatest compression angle θ_1 is chosen from one of the principles axis. Then optimum failure angle ψ_0 can be calculated from,

$$\psi_0 = \theta_1 \pm \beta . \qquad \textbf{4. 18}$$

Because the optimum planes are determined from σ_{ij}^{T}, normal and shear stress changes on optimum planes are calculated from σ_{ij}^{q}. The stress changes on optimum planes become

$$\sigma_{33} = \sigma_{xx}^{q}\sin^2\psi_0 - 2\sigma_{xy}^{q}\sin\psi_0\cos\psi_0 + \sigma_{yy}^{q}\cos^2\psi_0 \qquad \textbf{4. 19}$$

$$\tau_{13} = \frac{1}{2}\left(\sigma_{yy}^{q} - \sigma_{xx}^{q}\right)\sin 2\psi_0 + \tau_{xy}^{q}\cos 2\psi_0 \qquad \textbf{4. 20}$$

and the Coulomb stress change is

$$\sigma_f^{opt} = \sigma_{13} - \mu' \sigma_{33} \qquad \textbf{4. 21}$$

On the optimum planes, right and left lateral motions are the same respectively. At this point there is some point must be paid attention. Coulomb stress changes are calculated on optimum planes after earthquake. Optimum plane orientations are calculated from the total stress after earthquake. However, coulomb stress changes are caused by the stress changes on these planes.

Figure 4.3.b shows values of calculations to determine optimum orientations and Coulomb stress changes. Fault properties, elastic parameters and slip are the same as before. In addition, a uniform 10 MPa compressional stress is inserted to the calculations. White lines indicate the optimum right lateral orientation and the black ones, the optimum left lateral orientation. In this figure normal, shear and Coulomb stress changes are shown in separate panels.

a. Coulomb stress change for right-lateral faults parallel to master fault

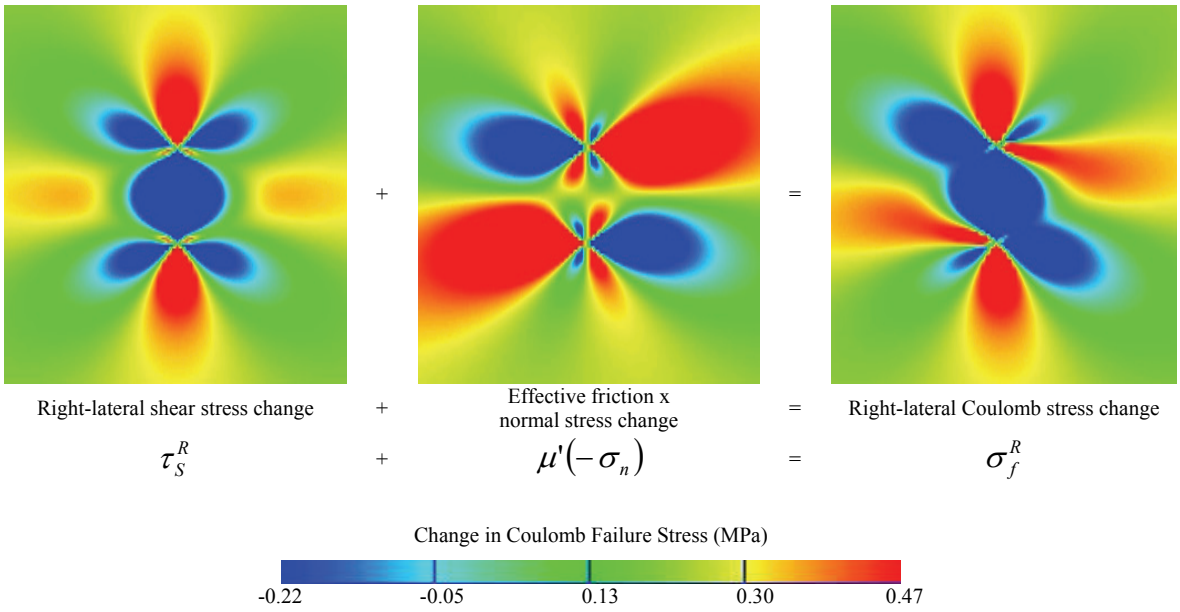

b. Coulomb stress change for faults optimally oriented for failure in a N27°E regional compressive stress (σ^r) of 10 MPa (King et. al., 1994)

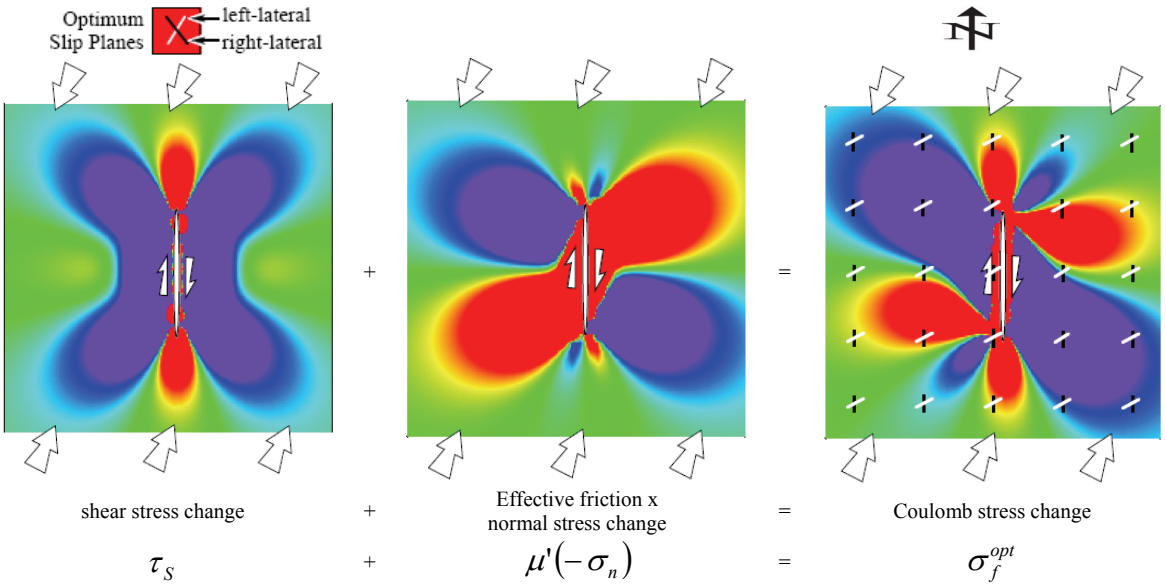

Figure 4.3 Illustration of the Coulomb stress change. Images show a map view of a vertical strike-slip fault embedded in an elastic half-space. Stress changes are depicted by graded colors. (a) Graphical presentation of equation 4.14 (b) Graphical presentation of equation 4.21

5. APPLICATION OF STRESS MODELING

5.1. Introduction

Angular dislocation method in an elastic half-space was used to calculate Coulomb failure stress changes (Yoffe, 1960; Comninou and Dunders, 1975). Poly3D is a C language computer program that calculates displacements, strains and stresses (Thomas, 1993). Fault models are defined as planar or polygonal elements in whole or half-space. Polygonal elements may have any number of sides, with a minimum of three. Geologically a polygonal element may represent a fracture or fault surface. Several or many elements may be used to model a fault with a non-uniform slip distribution. The polygonal elements in Poly3D are well suited for modeling complex surfaces with curving boundaries. Fault surfaces that change in both strike and dip can be meshed without creating gaps. Poly3D can calculate displacements, strains and stresses for each grid point on observation plane defined in input file.

5.2. Coulomb Stress Changes of the 2000 and 2002 Afyon Earthquakes

The models are parameterized by specifying the fault geometries, slip of the earthquakes and elastic parameters of the medium. The list of the parameters of S-1 and S-2 are given in Table 5.1. A Poisson's ratio (υ) of 0.25 and shear modulus (μ) was 33 MPa are assumed, respectively. An effective coefficient of friction is assumed 0.4. Values of 0.2 and 0.8 for the coefficient of friction resulted in Coulomb stress changes of ±0.03 MPa (±0.3 bar) different from the Coulomb stress changes computed using the value of 0.4 (Payne et al., 2004).

Coulomb failure stress analyses allowed evaluation of stress triggering of S-2 mainshock and S-3 on the Sultandağı Fault due to the: 1) S-1; 2) S-2 3) S-1 and S-2 combined.

S-1 is modeled as a single segment, 25 km length and 10 km, width (down-dip), and slip of 20 cm. The slip is estimated from seismic moment of 1.2 x 10^{18} N/m (NEIC-HRV).

S-2 is modeled as two segments 40 km of total length and 12 km width (down-dip), and a slip of 35 cm. The slip is estimated from seismic moment of 6 x 10^{18} N/m (NEIC-HRV).

Table 5-1 Fault model parameters for the Coulomb stress change calculations. (Focal mechanisms are from Harvard)

Earthquake →	**S-1**	**S-2**	**S-3**
Magnitude →	**M_w = 6.0**	**M_w = 6.5**	**M_w = 5.8**
Length (km)	25	40	8
Dip Slip (cm)	20	35	10
Strike (º)	285	269	236
Dip (º)	41	37	45
Rake (º)	-100	-71	-58
d_{min} (km)	0	0	0
d_{max} (km)	10	12	10
μ (Shear Modulus)	33 MPa		
υ (Poisson's Ratio)	0.25		

Figure 5.1 shows Coulomb stress changes due to S-1 mainshock without the effect of regional stress with the geometry of the rupture plane. Stress changes are calculated on the master fault at a depth of 8 km. Coulomb stress changes calculated on S-2 rupture plane is shown in Figure 5.2. The mainshock is located on the positive Coulomb values with maximum value of 4.4 bars. The seismic activity near Kızıldağ is too far to be affected by the Coulomb stress changes of S-1.

S-2 has a slightly different orientation and greater rupture length than S-1. The rupture started at the location where greatest positive Coulomb stress of S-1 rupture occurred. Figure 5.3 shows Coulomb stress changes due to S-2 mainshock without the effect of regional stress with the geometry of the rupture plane. Stress changes are calculated on the master fault at a depth of 8 km. Coulomb stress changes calculated on S-3 rupture plane is shown in Figure 5.4 and on auxiliary plane is shown in Figure 5.5.

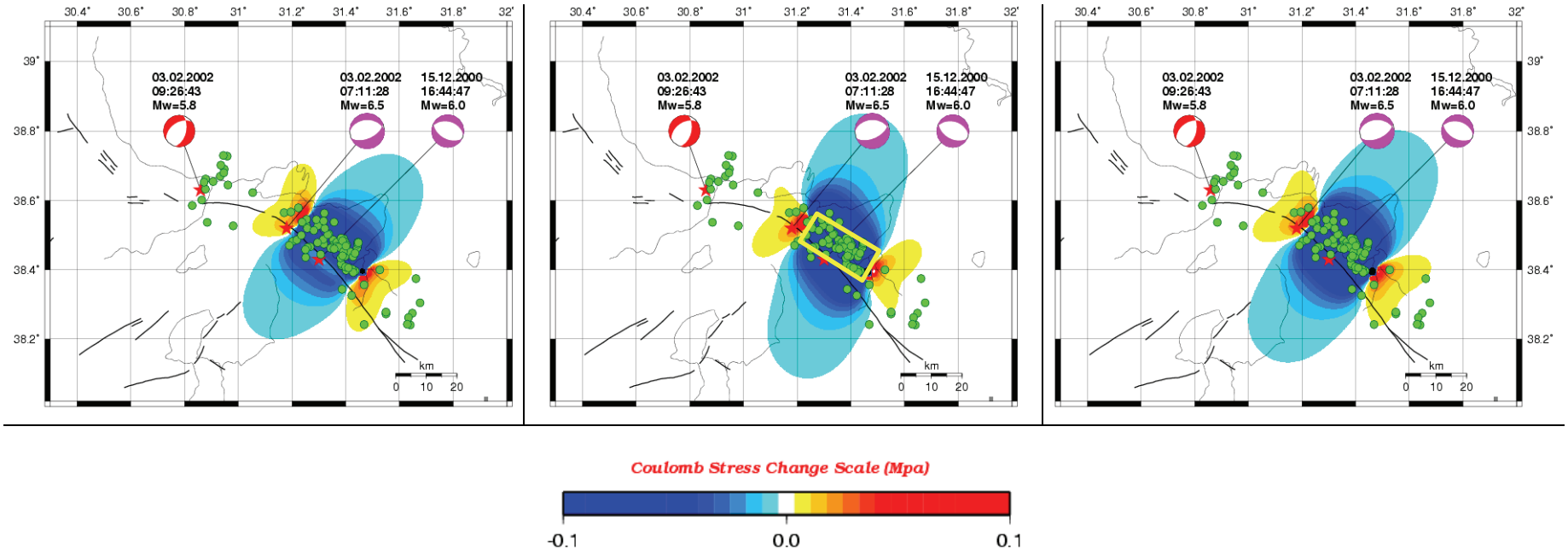

Shear Stress Change	Normal Stress Change	Coulomb Stress Change
τ_S	σ_n	σ_f

Figure 5.1 Shear, Normal and Coulomb stress changes due to S-1 mainshock without the effect of regional stress. Stress changes are resolved on infinitesimal, subparallel receiver faults at selected depth of 8 km. S-1 mainshock is modeled as one fault plane (yellow box) described in the text and its position relative to the faults. Green circles indicate relocated aftershocks and stars are the mainshock locations. Focal mechanisms are from Harvard.

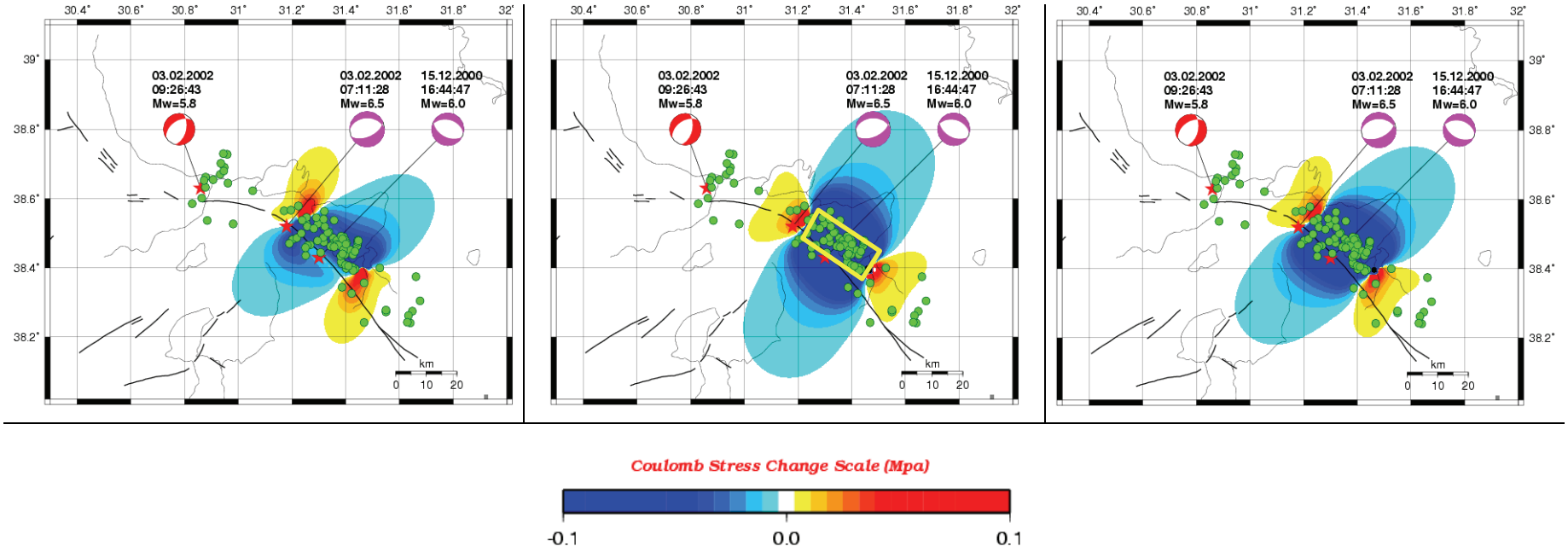

Shear Stress Change	Normal Stress Change	Coulomb Stress Change
τ_S	σ_n	σ_f

Figure 5.2 Map view shows stress changes at selected depth for specified orientations of normal faults: 8 km depth for the orientation of the mechanism of S-2 mainshock with strike N269E, dip 37NE, and rake -71. S-1 mainshock is modeled as one fault plane (yellow box) described in the text and its position relative to the faults. Green circles indicate relocated aftershocks and stars are the mainshock locations. Focal mechanisms are from Harvard.

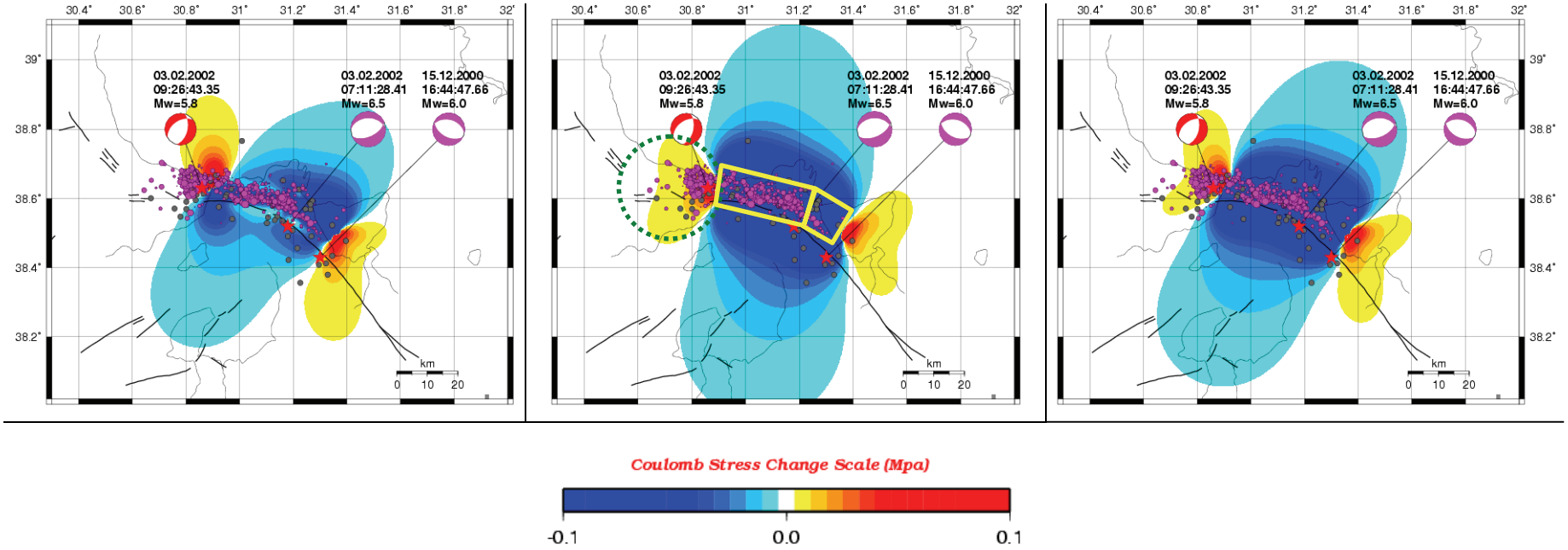

Shear Stress Change	Normal Stress Change	Coulomb Stress Change
τ_S	σ_n	σ_f

Figure 5.3 Coulomb stress changes due to S-2 mainshock without the effect of regional stress. Stress changes are resolved on infinitesimal, subparallel receiver faults at the depth of 8 km. S-2 mainshock is modeled as two segments (yellow boxes). Dark grey circles indicate relocated aftershocks; circles are the locations from TÜBİTAK-MRC aftershock study and stars are the mainshock locations. Focal mechanisms are from Harvard.

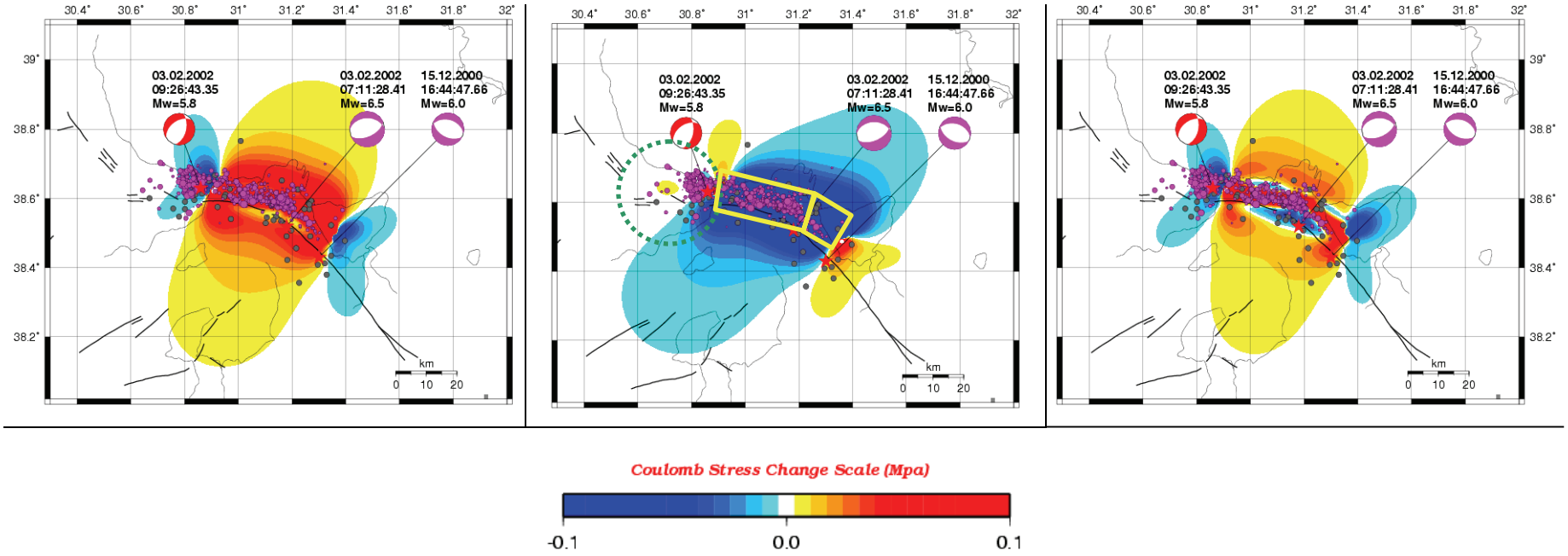

Shear Stress Change	Normal Stress Change	Coulomb Stress Change
τ_S	σ_n	σ_f

Figure 5.4 Map view shows stress changes at selected depth for specified orientations of normal faults: 8 km depth for the orientation of the mechanism of the largest aftershock of S-2 with strike N236E, dip 45NE. The region is bounded with a green dashed line. S-2 mainshock is modeled as two fault planes (yellow boxes) described in the text and its position relative to the faults. Dark grey circles indicate relocated aftershocks, circles are the locations from TÜBİTAK-MRC aftershock study and stars are the mainshock locations. Focal mechanisms are from Harvard.

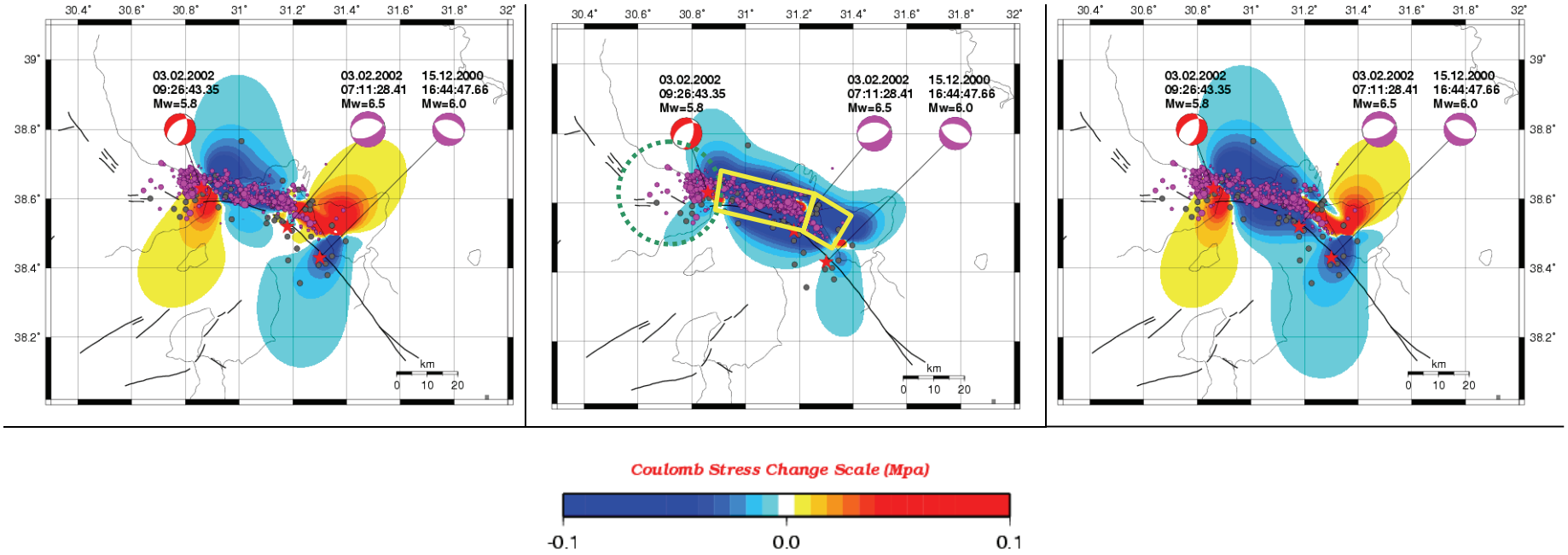

Shear Stress Change	Normal Stress Change	Coulomb Stress Change
τ_S	σ_n	σ_f

Figure 5.5 Map view shows stress changes at selected depth for specified orientations of normal faults: 8 km depth for the orientation of the mechanism of the largest aftershock of S-2 with strike N15E, dip 53NE. The region is bounded with a green dashed line. S-2 mainshock is modeled as two fault planes (yellow boxes) described in the text and its position relative to the faults. Dark grey circles indicate relocated aftershocks, circles are the locations from TÜBİTAK-MRC aftershock study and stars are the mainshock locations. Focal mechanisms are from Harvard.

The results of the Coulomb stress calculations show that the 2002 Sultandağı earthquake (S-2) is located in a region of increased Coulomb stress greater than 0.4 MPa, resulting from the 2002 earthquake (S-1). Previous studies on the mainshock-aftershock sequences suggest static stress increases as low as 0.01 MPa can encourage failure on nearby faults (Reasenberg and Simpson, 1992; King et al., 1994). Since both S-1 and S-2 are related to the segments of the same fault, it is expected that the conditions for the stress triggering is favorable. However, it is important to ask the question why the rupture of 2000 event stopped at the location of the 2002 event. There might be several different mechanisms acting alone or simultaneously. It is obvious that the fault geometry is significantly changing from southeast to northwest. It is known from the observations and model studies that the changes in the geometry of fault may stop the rupture and the termination of the rupture is the region of increased stress. Another mechanism would be to assume the presence of asperity or barrier at the termination of the rupture. An asperity can act as a barrier for the termination of the rupture and then rupture with greater stress drop.

The activity observed in the region of the S-3 earthquake cannot be explained by the Coulomb stress change since the distance is too large. The activity started several weeks later than S-1 earthquake. A plausible mechanism would be dynamic triggering as result of shear strain during the earthquake. However, there is no straightforward mechanism to explain the delay of the activity.

The activity in the region of S-3 was also observed following the S-2 event. S-3 with magnitude 5.8 occurred few hours later. The Coulomb stress calculations, which resolved on both probable fault mechanisms of S-3 reported by Harvard, show a decrease on shear, and Coulomb stresses in Figure 5.4 and normal stress in Figure 5.5. However, in Figure 5,4 normal stress and in Figure 5.5, shear and Coulomb stresses increases in the activity area. The normal stress decrease and increase in Coulomb stress create a favorable environment for the triggering of the S-3 event. We observed this situation in Figure 5.5, but we know from the morphology of the area, the mechanism of S-3 with strike 236° is appropriate for the rupture. In addition, the dynamic triggering mechanism would be a possible mechanism for the occurrence of the S-3 earthquake and the related activity. According to Steacy et al. (2005) dynamic and static stress changes cannot be distinguished either observationally or

theoretically at short times and distances from an earthquake, and both attenuate approximately as some inverse power of the distance. Static stress changes attenuate more rapidly, roughly inversely to the cube of the distance from the causative fault, while dynamic stress changes attenuate more slowly and therefore dominate at large distances. When we are taking into account all this, we can say that both static and dynamic triggering mechanism can be possible for the triggering S3 and the aftershock which occur in that area due to S2.

6. DISCUSSION AND CONCLUSIONS

The main goal of this study is to investigate the fault interaction through elastic stress transfer among the Sultandağı earthquakes (S-1, S-2 and S-3). We examined the spatial pattern of aftershocks and analyzed Coulomb stress changes caused by the mainshocks.

We relocated the mainshocks and aftershocks of both events using relative location and cross-correlation techniques. The relocated events and the results of the aftershock study performed by TÜBİTAK-MRC lead to the following conclusions;

- The aftershock locations of S-1 show that the rupture started on the southeastern part of the fault and propagated to the northwest.
- The length of the rupture is approximately 25 km and consistent with the moment magnitude estimate assuming 20 cm of slip.
- An activity approximately 40 km from the termination of S-1 was observed three months after the mainshock.
- The aftershock study from TÜBİTAK-MRC provided a better estimate of the seismic moment and the rupture geometry for S-2.
- The length of the rupture for S-2 is estimated as 40 km from the seismicity, which is in agreement with the moment magnitude with a slip of 35 cm.
- The rupture approximately started at the termination of S-1 and propagated to the northwestern termination of the fault.
- An activity similar to the one observed during S-1 took place at the termination of the rupture and S-3 event occurred within this activity.

The modeling studies for the directivity indicate that both ruptures almost propagated unilaterally to the northwest. This is consistent with the aftershock distributions and the locations of the mainshocks obtained in this study.

Based on the seismicity, fault plane solutions, and the locations of the mainshocks and the result of the directivity studies we constructed simple fault models for S-1 and S-2. The Coulomb failure stress is calculated in an elastic half space using a boundary element technique from the fault geometries of S-1 and S-2.

Both S-1 and S-2 have similar normal mechanism with slightly different strikes. Therefore, the segment of the fault ruptured during S-2 is favorable oriented for the stress field from S-1. The calculated Coulomb stress changes indicate that the segment of the fault related to S-2 rupture area is exposed to a maximum stress increase of 4 bars as a result of S-1.

Following both earthquakes, Seismic activities were observed 40 km away from S-1 mainshock and 25 km away from S-2 mainshock. The Coulomb stress as a result of S-1 cannot be responsible for the observed increase of activity since the distance is too large. The dynamic triggering is plausible mechanism to explain the activity. However, since the activity started 3 months later than the main shock a delaying mechanism for the increased activity must be considered. A similar activity in the same area was also observed few hours following S-2. The Coulomb stress calculations show a decrease on the normal stress in the area of the triggered activity. Since the strike of S-3 is almost perpendicular to S-2, the decrease on the normal stress and increase on the Coulomb stress might favor the S-3. Therefore, we conclude that the activity in the region of S-3 might occur as a result of static and dynamic triggering.

7. REFERENCES CITED

Ambraseys, N. N., 1970, *Some characteristic features of the Anatolian fault zone*, Tectonophysics, 9, 143-165.

Angelier, J., 1978, *Tectonic evolution of the Hellenic Arc since the Late Miocene*, Tectonophysics, 49, 23-36.

Barka A., Kadinski-Cade K., 1988, *Strike-slip fault geometry in Turkey and its influence on earthquake activity*, Tectonophysics, 7, 663-684.

Barka, A., Reilinger, R., Şaraoğlu, F., Şengör, A.M.C., 1995, *Proceedings of the International Earth Science Colloquium on the Aegean Region*, 1, 3-18.

Boray, A., Şaraoğlu, F., Emre, Ö., 1985, Jeoloji Mühendisliği, 23, 9-20.

Bouchon, M., 1981, *A simple method to calculate Green's function in elastic layered media*, BSSA. 71, 959-971.

Bozkurt, E., 2001, *Neotectonics of Turkey - a synthesis*, Geodinamica Acta, 14, 3-30.

Çağatay, M. N., Görür, N., Alpar, B., Saatçılar, R., Akkök, R., Sakınç, M., Yüce, H., Yaltırak, C., Kuşcu, İ., *Geological evolution of the Gulf of Saros, NE Aegean Sea*, 1998, Geo-Marine Letters, ISSN: 0276-0460, 17: 1-9.

Carder, D.S., 1945, *Seismic investigations in the Boulder Dam area, 1940–1945, and the influence of reservoir loading on earthquake activity,* BSSA, v. 35.

Cocco M., King G.C.P. and Nostro, C., 1999, *Fault Interaction and Stress Changes: Recent Advances and New Horizons, Report for the F.A.U.S.T Project*, Alicante, January.

Comninou, M. A. and Dunders, J., 1975, *The angular dislocation in a half-space*, Journal of Elasticity, v. 5, p. 203-216.

Das, S. and Scholz, C. H., 1983, *Why large earthquakes do no nucleate at shallow depths*, Nature, 305, 621–623.

Das, S. and Scholz, C. H., 1981, *Off-fault aftershock clusters caused by shear stress increase?,* Bull. Seismol. Soc. Am., 71, 1669-1675.

Deng, J., and Sykes, L. R., 1997a, *Evolution of the stress field in southern California and triggering of moderate-size earthquakes: A 200-year perspective*, J. Geophys. Res., 102, 9859-9886.

Deng, J., and Sykes, L. R., 1997b, *Stress evolution in southern California and triggering of moderate-, small-, and micro-size earthquakes*, J. Geophys. Res., 102, 24,411-24,435.

Dewey, J. F. and Şengör, A. M. C., 1979, *Aegean and surrounding regions: Complex multiplate and continuum tectonics in a convergent zone*, Geological Soc. of Am. Bull., Vol. 90, pp. 84-92.

Nalbant S. S., McCloskey, J., Steacy, S. and Barka, A. A., 2002, *Stress accumulation and increased seismic risk in eastern Turkey*, Earth and Planetary Science Letters, Volume 195, Issues 3-4, Pages 291-298.

Erdik, M., Sesetyan, K., Demircioglu, M.B., Celep, U., Biro, Y., Uckan, E., 2002, *Sultandağı Earthquake Report– Turkey*, Department of Earthquake Engineering, Kandilli Obs. and Earthquake Res. Ins., Bogazici University.

Gomberg, J. 1996 *Stress/strain changes and triggered seismicity following the Mw 7.3 Landers, California, earthquake,* J. Geophys. Res., Vol. 101, No. B1, p. 751-764 (95JB03251).

Gomberg, J., Beeler, N. M., Blanpied, M. L., and Bodin, P., 1998, *Earthquake triggering by transient and static deformations*, J. Geophys. Res., 103, 10, 24,411-24,426.

Harris, R. A., *Introduction to special section: Stress triggers, stress shadows, and implications for seismic hazard*, J. Geophys. Res., 103 , 10 , 24,347-24,358, 1998.

Healy, J.H., Rubey, W.W., Griggs, D.T. and Raleigh C.B., 1968, *The Denver earthquakes*, Science, 161, 1,301-1,310.

Hill, D.P., P.A. Reasemberg, A. Michel, W.J. Arabasz, G. Beroza, D. Brunbaugh, J.N. Brune, R. Castro, S. Davis, D. de Polo, W.L. Ellsworth, J. Gomberg, S. Harmsen, L. House, S.M. Jackson, M. Johnston, L. Jones, R. Keller, S. Malone, L. Munguia, S. Nava, J.C. Pechman, A. Sanford, R.W. Simpson, R.S. Smith, M. Stark, M. Stickne, A. Vidal, S. Walter, V. Wong, and J. Zollweg, 1993, *Seismicity remotely triggered by the magnitude 7.3 Landers, California, earthquake*, Science, 260, 1617-1623.

Hillers, G., 2001, *Earthquake probability calculations based on Coulomb Stress modeling applied to mapped faults inside the Sea of Marmara*, Master thesis, Ruhr-University Bochum.

Hodgkinson, K. M., Stein, R. S., and King, G. C. P., 1996, *The 1954 Rainbow Mountain-Fairview Peak-Dixie Valley earthquakes: A triggered normal faulting sequence*, J. Geophys. Res., 101, 25,459-25,471.

Hubert-Ferrari, A., Barka, A. A., Jacques, E., Nalbant, S. S., Meyer, B., Armijo, R., Tapponier, P. and King., G. C. P., 2000, *Seismic hazard in the Marmara Sea region following the 17 August 1999 İzmit earthquake*. Nature, 404(6775):269–273.

Jackson, J. and McKenzie, D., 1984, *Active tectonics of the Alpine–Himalayan belt between western Turkey and Pakistan*, Geophys. J. R. Astr. Soc., 77, pp. 185-264.

Jaeger, J. C., and Cook, N. G. W., 1979, *Fundamentals of Rock Mechanics*, 3rd ed., 593+XXII pp. Chapman and Hall, London.

Ketin, I., 1948, *Uber die tektonisch-mechanischen Folgerungen aus den grossen anatolischen Erdbeben des letzten Dezenniums*, Geol. Rundsch., 36, 77-83.

Ketin, I., 1968, *Relations between General Tectonic Features and the Main Earthquake Regions of Turkey*, Bull. of Mineral. Research and Expl. Inst., 72, pp. 1-28, Ankara.

Kilb, D., Gomberg, J., Bodin, P., 2002, *Aftershock triggering by complete Coulomb stress changes*, J. Geophys. Res, VOL. 107, NO. B4, 2060, 10.1029/2001JB000202.

King, G. C. P. and Cocco, M., 2000. *Fault interaction by elastic stress changes: new clues from earthquake sequences*, Advances in Geophysics, 44, 1–38.

King, G.C.P, Stein, R.S. and Lin, J., 1994, *Static Stress Changes and the Triggering of Earthquakes*, BSSA, v. 84, No. 3, pp. 935-953.

Kiratzi, A. and Louvari, E., 2003. *Focal mechanisms of shallow earthquakes in the Aegean Sea and the surrounding lands determined by waveform modeling: a new database*, Journal of Geodynamics, 36, 251 - 274.

Kissling, E., Ellsworth, W. L., Eberhart-Phillips, D., and Kradolfer U., 1994, *Initial reference models in local earthquake tomography*, J. Geophys. Res. 99, 19635-19646.

Kocyigit; A., Unay, E., and Sarac, G., 2000, GSA Special Publ., pp173,405-421

Le Pichon, X., Angelier, J. J., 1981, *The Aegean Sea*, Phil. Trans. R. Sot., 300, 357-372.

Lee, W.H.K., and Lahr, J.C., l975, *HYPO7l (Revised): A computer program for determining hypocenter, magnitude, and first motion pattern of local earthquakes*, U.S. Geological Survey Open-file Report 75-3ll, ll3 p.

Lienkaemper, J. J., and Galehouse, J. S., 1997, *Revised long-term creep rates on the Hayward Fault, Alameda and Contra Costa Counties*, California, U.S. Geol. Surv., Open-File Rep. 97-690, 18.

Lin, J., and Stein, R. S., 2004, *Stress triggering in thrust and subduction earthquakes and stress interaction between the southern San Andreas and nearby thrust and strike-slip faults*, J. Geophys. Res., VOL. 109, B02303, doi:10.1029/2003JB002607.

McGarr, A., and Simpson, D., 1997, *A broad look at induced and triggered seismicity, in Rockbursts and Seismicity in Mines*, edited by S. Lasocki and S. Gibowicz, pp. 385-396, A. A. Balkema, Rotterdam, Netherlands.

Nalbant, S. S., Hubert, A., and King, G. C. P., 1998, *Stress coupling between earthquakes in northwest Turkey and the north Aegean Sea*, J. Geophys. Res., 103, 10, 24,469-24,486.

Nalbant,. S.S., McCloskey, J., Steacy, S., Barka, A.A., 2002, *Stress accumulation and increased seismic risk in eastern Turkey*, Earth and Planetary Science Letters, 195, 291-298.

Nostro, C., Chiaraluce, L., Cocco, M., Boumont, D., and Scotti, O., 2005, *Coulomb stress changes caused by repeated normal faulting earthquakes during the 1997– 1998 Umbria-Marche (central Italy) seismic sequence*, J. Geophys. Res., 110, B05S20, doi:10.1029/2004JB003386.

Özgül, N., Bölükbaşı, S., Alkan, H., Öztaş, Y. ve Korucu, M., 1991, *Göller bölgesinin tektonostratigrafik birlikleri,* O. Sungurlu sempozyumu bildirileri, Ankara, 213-237.

Parsons, T., Toda, S., Stein, R. S., Barka, A., and Dieterich, J. H., 2000, *Heightened odds of large earthquakes near Istanbul: an interaction-based probability calculation*, Science, 288 (5466):661–665.

Payne, S. J., Zollweg, J. E., and Rodgers, D. W., 2004, *Stress Triggering of Conjugate Normal Faulting: Late Aftershocks of the 1983 Ms 7.3 Borah Peak, Idaho, Earthquake*, BSSA, Vol. 94, No. 3, pp. 828–844.

Pınar, A., Honkura, Y., and Kuge, K, 2001, *Seismic activity triggered by the 1999 İzmit earthquake and its implications for the assessment of future seismic risk*. Geophys. J. Int., 146(1):F1–F7.

Raleigh, C.B., Healy, J.H., and Bredehoeft, J.D., *Faulting and Crustal Stress at Rangely, Colorado, Flow and Fracture of Rocks*, Geophysical Monograph #16, American Geophysical Union (Heard, et al ed. 1972)

Reasenberg, P. A., and Simpson, R. W., 1992, *Response of regional seismicity to the static stress change produced by the Loma Prieta earthquake*, Science, 255, 1687-1690.

Reilinger, R., Simon McClusky, Philippe Vernant, and Shawn Lawrence, Semih Ergintav and Rahsan Cakmak, Fakhraddin Kadirov and Ibrahim Guliev, Ruben Stepanyan, Merab Nadariya and Galaktion Hahubia, Salah Mahmoud, and K. Sakr, Abdullah ArRajehi, Demitris Paradissis, A. Al-Aydrus, Mikhail Prilepin and Tamara Guseva, Emre Evren, Andriy Dmitrotsa and S.V. Filikov, Francisco Gomez, Riad Al-Ghazzi, Gebran Karam, 2006, *GPS Constraints on Continental Deformation in the Africa-Arabia-Eurasia Continental Collision Zone and Implications for the Dynamics of Plate Interactions*, submitted.

Rybicki, K., 1973, *Analysis of aftershocks on the basis of dislocation theory*, Phys. Earth Planet. Inter., 7 , 409-422.

Sanders, C. O., 1993, *Interaction of the San Jacinto and San Andreas fault zones, Southern California; triggered earthquake migration and coupled recurrence intervals*, Science, v. 260, p. 973-976.

Şaroğlu, F., Emre, Ö., and Boray, A., 1987, *MTA Report*, No:8174.

Segall, P., 1992, *Induced stress due to fluid extraction from axsymmetric reservoirs*, Pure Appl. Geophys., 139, 535-560.

Şengör, A. M. C., 1984, The *Cimmeride orogenic system and the tectonics of Euraisa*, Geol. Soc. America Spec. Paper., 195, xi+82.

Şengör, A.M.C., 1979, *The North Anatolian transform fault: Its age, offset and tectonic significance*, J. Geol. Soc. London, 136, 269-282.

Şengör, A.M.C., Görür, N. and Şaroğlu, F., *1985, Strike-slip faulting and related basin formation in zones of tectonic escape: Turkey a case study: in Biddle, K.T. and Christie-Blick, N., edts, Strike-slip Deformation, basin Formation, and Sedimentation*, Soc. Econ. Paleont.Min.Spec.Pub. 37 (in honor of J.C. Crowell), p. 227-264.

Simpson, R. W., and P. A. Reasenberg, 1994, *Earthquake-induced static stress changes on central California faults, in The Loma Prieta, California Earthquake of October 17,*

1989—Tectonic processes and models, edited by R. W. Simpson, U.S. Geol. Surv. Prof. Pap., 1550-F, F55-F89.

Smith, S.W., and Lindt, W. V., 1969, *Strain adjustments associated with earthquakes in Southern California*. Bull. Seismol. Soc. Am. 59 (1969), pp. 1569–1589.

Sanders, C.O., 1993, *Interaction of the San Jacinto and San Andreas Fault zones, southern California: triggered earthquake migration and coupled recurrence intervals*: Science, v. 260, p. 973-976.

Stein, R. S., 1999, *The role of stress transfer in earthquake occurrence*, Nature, 402, 605–609.

Stein, R. S. and Hanks, T. C., 1998, *M 6 earthquakes in southern California during the twentieth century: no evidence for a seismicity or moment deficit*, Bull. Seism. Soc. of America, 88(3):635–652.

Stein, R. S., Barka, A. A., and Dieterich, J. H., 1997, *Progressive failure on the North Anatolian fault since 1939 by earthquake stress triggering*, Geophys. J. Int., 128, 594-604.

Stein, R. S., and Lisowski, M., 1983, *The 1979 Homestead Valley earthquake sequence, California: Control of aftershock and postseismic deformation*, J. Geohys. Res., 88, pp. 6477-6490.

Stein, R. S., 2005, *Earthquake Conversations*, Scientific American, vol. 288, pp. 72-79, January issue,2003. Also published in: Our Ever Changing Earth, Scientific American, Special Edition, v. 15 (2), pp. 82-89.

Taymaz, T., Jackson, J.A., and McKenzie, D., 1991, *Active Tectonics of the North and Central Aegean Sea*, Geophysical Journal International-Oxford, 106, 433-490.

Utkucu M., Nalbant, S.S., McCloskey, J., Steacy, S. and Alptekin, Ö., 2003, *Slip distribution and stress changes associated with the 1999 November 12, Düzce (Turkey),* Geophys. J. Int., 153 (1), 229-241.

Wyss, M., Brune, J. N., 1967, The Alaska Earthquake of 28 March 1964: A complex multiple rupture, Bull. Seism. Soc. of America, 57(5):1017-1023.

Yamashina, K., 1978, *Induced earthquakes in the Izu Peninsula by the Izu-Hanto-Oki earthquake of 1974, Japan*, Tectonophysics, 51, 139–154.

Yoffe, E. H., 1960, The angular dislocation: Philosophical Magazine, 5, 161-175.

INDEX

APPENDIX A: AZIMUTH AND DISTANCE OF THE STATIONS, WHICH ARE USED FOR RELATIVE LOCATION.

Station Code	For 2000 Mw=6.0		For 2002 Mw=6.5	
	Azimuth (Degree)	Distance to event (km)	Azimuth (Degree)	Distance to event (km)
KON	123	115	120	104
ISP	221	100	227	97.4
MUD	359	217	357	227
KHL	263	153	267	159
CAN	40	308	38	312
IZI	323	255	324	266
SAF	21	326	20	334
DST	299	258	300	269
HRT	332	291	332	303
KCT	309	317	310	328
YER	241	304	243	304
BNT	306	353	307	364
BOY	41	444	40	448
CTT	321	380	321	392
CSS	154	435	154	423
HTY	120	507	119	496
EIL	160	1038	160	1026
FURI	165	3360	165	3349
CHTO	88	6814	88	6808
GVD	240	760	241	760
SKD	244	738	245	739

APPENDIX B: EARTHQUAKE FOCAL MECHANISMS SHOWED IN FIGURE 3.2.

NO	Date (YYMMDD)	Time (Hour:Min:Sec)	Latitude E	Longitude N	Depth (Km)	M_w	Nodal Plane 1			Nodal Plane 2		
							Strike (Degree)	Dip (Degree)	Rake (Degree)	Strike (Degree)	Dip (Degree)	Rake (Degree)
1	800502	05:31:10	36.35	29.39	22.0	5.6	94	75	104	230	20	48
2	861011	09:00:12	37.91	28.53	9.0	5.7	325	42	-36	83	67	-126
3	890427	23:06:53	37.10	28.20	7.0	5.3	271	57	-103	114	35	-71
4	890428	13:30:20	37.06	28.01	22.0	5.3	271	58	-103	115	34	-70
5	900718	11:29:26	37.04	29.51	14.0	5.4	270	41	-60	53	55	-113
6	921106	20:06:02	38.02	26.97	6.0	6.0	146	76	13	53	77	166
7	940128	15:45:26	38.67	27.48	14.0	5.3	259	35	-120	114	60	-71
8	940524	02:05:39	38.83	26.49	10.0	5.5	256	60	-131	136	49	-41
9	960402	07:59:26	37.84	26.87	9.0	5.3	261	53	-119	124	46	-57
10	960720	00:00:40	36.07	27.46	12.0	6.1	232	42	-52	6	58	-119
11	790614	11:44:46	38.80	26.60	8.0	5.8	262	41	-108	105	51	-75
12	951001	15:57:16	38.06	30.13	4.0	6.3	136	43	-87	312	47	-93
13	550716	07:07:00	37.66	27.19	10.0	6.8	55	51	-133	291	55	-50
14	560220	20:31:00	39.86	30.49	10.0	6.2	140	56	-51	265	50	-133
15	570424	19:10:13	36.40	28.60	1.0	6.8	83	63	28	339	65	150
16	570425	02:25:42	36.50	28.60	1.0	7.2	58	85	19	326	71	175
17	590425	00:26:00	37.00	28.50	1.0	6.2	65	76	-70	189	24	-144
18	681205	07:52:00	36.60	26.90	7.0	6.0	57	46	-72	212	47	-108
19	690114	23:12:00	36.10	29.20	10.0	6.3	100	74	82	307	18	116
20	690406	03:49:00	38.50	26.40	16.0	5.9	116	60	-90	296	30	-90
21	690430	20:20:32	39.10	28.50	8.0	5.4	78	39	-114	288	55	-72
22	700328	23:11:00	39.10	29.60	10.0	5.5	277	60	-78	74	32	-110
23	700423	09:01:00	39.08	28.60	30.0	5.6	77	50	-96	266	40	-83
24	710512	10:10:26	37.60	29.70	2.0	5.1	214	89	-90	28	1	-96
25	720314	14:05:00	39.30	29.46	18.0	5.6	101	35	-87	277	55	-92
26	871005	09:27:02	36.25	28.28	29.0	5.1	38	55	170	134	82	35
27	650613	20:01:51	37.80	29.30	2.0	5.9	91	74	-103	311	21	-52
28	690323	21:08:42	39.10	28.50	8.0	5.9	112	34	-90	292	56	-90
29	690325	13:21:34	39.20	28.40	8.0	6.1	90	40	-104	288	51	-79
31	700328	21:02:23	39.20	29.50	7.7	7.1	304	41	-97	133	49	-84
32	700416	10:42:24	38.97	29.92	8.0	5.6	280	31	-100	112	60	-84
33	700419	13:29:38	39.00	29.80	9.0	6.1	104	43	-90	284	47	-90
34	710512	06:25:13	37.57	29.70	12.0	5.8	230	35	-105	68	56	-80
35	710512	12:57:23	37.60	29.60	12.0	5.5	235	65	-89	53	25	-92
36	710525	05:43:28	39.07	29.67	6.0	5.9	298	55	-77	96	37	-108
37	750430	04:28:57	36.18	30.77	25.0	5.4	109	80	70	353	22	152
38	760819	01:12:37	37.70	28.89	4.0	6.1	276	69	-131	164	45	-30